Summer Climate Variability in the North Atlantic-European region

C. Ole W. WULFF
(Matrikelnummer: 5478)

MASTER THESIS

submitted in fulfilment of the requirements for the degree

Master of Science (M.Sc.)
Climate Physics: Meteorology and Physical Oceanography

at the Faculty of Mathematics and Natural Sciences
Christian-Albrechts-Universität zu Kiel
GEOMAR Helmholtz Centre for Ocean Research Kiel

First supervisor: Prof. Dr. rer. nat. Richard GREATBATCH
Second supervisor: Prof. Dr. Daniela DOMEISEN

Kiel, May 4, 2017

Abstract

The increasing number of climatically exceptional summers in the past two decades has drawn researchers' interest to the characteristics of summer variability and its prediction. In this thesis, the atmospheric summer variability of the North Atlantic-European (NAE) sector is examined. Applying a Principal Component Analysis to reanalysis data of seasonal geopotential height anomalies at 500 hPa, two dominant modes are identified - the summer North Atlantic Oscillation (SNAO) and the summer East Atlantic (SEA) mode. The former is associated with a latitudinal shift of the jet stream but unlike its winter counterpart also impacts the meridional component of the flow. The latter is part of a zonal wave number 5 wave train and is associated with significant anomalies in meridional flow and meandering of the jet. Both modes are shown to have significant impacts on the surface climate of the NAE sector. The controls are mainly through cloud cover anomalies associated with the large-scale rising/sinking motions in their main centres of action and temperature and moisture advection by the anomalous geostrophic flow.

In order to examine the potential for prediction of the NAE summer variability, seasonal hindcast experiments are carried out with an atmospheric model applying a relaxation technique in different regions of the atmosphere. The aim of these is to show from which parts of the climate system predictability of summer variability can arise. For the SNAO, no potential for an improved prediction of its interannual variability can be found from any of the forcing regions. Even though previous modelling and observational studies show that the long-term variability of the SNAO is controlled by the Atlantic multidecadal variability, the experiments do not confirm this link.

For the SEA, the experiments indicate that no forcing is included in the relaxation regions but that predictability arises from the prescription of observed anomalous lower boundary conditions. Further investigation reveals that this is the result of diabatic heating anomalies in the Caribbean and the tropical Pacific driven by anomalous sea surface temperatures. As a consequence, the upper tropospheric flow is altered in the tropics but also further north where it can interact with the jet stream. This anomalous divergent flow acts as a source for Rossby waves in the eastern North Pacific which can propagate downstream in the jet stream wave guide. The resulting stationary wave train projects onto the SEA pattern in the NAE region. This tropical-extratropical teleconnection offers potential for enhanced predictability of the SEA mode.

Since experiments with tropical relaxation quite accurately reproduce the diabatic forcing but cannot predict the SEA variability, it is clear that the application of the relaxation technique constitutes a problem. It is hypothesised that the failure at simulating the correct planetary wave propagation is attributable to altered dissipation properties in the relaxation zone.

Zusammenfassung

Die Struktur der atmosphärischen Sommerzirkulation und ihre Vorhersage haben erst mit dem vermehrten Auftreten von Extremereignissen wie Hitzewellen und Dürren in den letzten zwei Jahrzehnten an Aufmerksamkeit in der Klimaforschung gewonnen. In dieser Arbeit wird die Variabilität der Atmosphäre im Sommer im Nordatlantisch-Europäischen (NAE) Raum untersucht. Mittels einer Hauptkomponentenanalyse des saisonal gemittelten Geopotentials auf 500 hPa aus Reanalysedaten werden zwei vorherrschende Zirkulationsmuster identifiziert - die summer North Atlantic Oscillation (SNAO) und die summer East Atlantic (SEA) Mode. Die SNAO geht einher mit einer nord-süd Verschiebung des Strahlstroms. Anders als ihr Pendant in den Wintermonaten beinhaltet sie darüber hinaus eine meridionale Komponente. Die SEA Mode ist Teil eines planetaren Wellenzuges und verursacht signifikante Anomalien der meridionalen Winde und folglich ein Mäandrieren des Strahlstroms. Beide Muster haben Einfluss auf Bodentemperaturen und Niederschlag im NAE Raum. Dabei sind sowohl die Advektion von Temperatur und Feuchte als auch Anomalien in der Bewölkung, die im Zusammenhang mit großskaligen Hebungs- und Absinkbewegungen in den Zentren der Muster stehen, von Relevanz.

Um das Vorhersagepotential der Sommervariabilität im NAE Raum zu untersuchen, werden saisonale retrospektive Vorhersageexperimente mit einem Atmosphärenmodell durchgeführt, in denen eine Relaxationsmethode in verschiedenen Regionen der Atmosphäre angewandt wird. Ziel dieser ist es, zu zeigen, in welchen Teilen des Klimasystems Vorhersagbarkeit ihren Ursprung hat. Für die SNAO kann dabei kein Potential für eine verbesserte Vorhersage aus den Relaxationsregionen abgeleitet werden. Obwohl frühere Modell- und Beobachtungsstudien gezeigt haben, dass die SNAO auf großen Zeitskalen dem Einfluss der Atlantischen, multidekadischen Temperaturvariabilität unterliegt, wird die durch die Experimente nicht bestätigt.

Für die SEA Mode zeigen die Experimente, dass die Relaxationsregionen keinen Antrieb beinhalten, sondern dass Vorhersagbarkeit aus dem Vorschreiben von beobachteten Anomalien als untere Randbedingungen resultiert. Durch weitere Analysen stellt sich heraus, dass dies das Resultat diabatischer Erwärmung im Zusammenhang mit den Anomalien der Meeresoberflächentemperaturen ist. Dessen Konsequenz ist eine Modifikation der Strömung in der oberen Troposphäre sowohl in den Tropen, als auch weiter nördlich, wo sie mit dem Strahlstrom wechselwirkt. Diese Anomalien der divergenten Strömungskomponente agiert als Quelle für Rossbywellen im östlichen Nordpazifik, die im Wellenleiter des Strahlstroms stromabwärts propagieren können. Der resultierende stationäre Wellenzug ähnelt im NAE Raum dem SEA Muster. Diese tropisch-extratropische Fernwechselwirkung birgt Potential für eine verbesserte Vorhersage der SEA Mode.

Da die Experimente mit tropischer Relaxation den Ursprung dieser Telekonnektion korrekt wiedergeben, aber die Variabilität der SEA Mode nicht vorhersagen können, muss die Anwendung der Relaxationsmethode das Problem darstellen. Es

wird gemutmaßt, dass der Grund für das Scheitern der Vorhersage der korrekten planetaren Wellenausbreitung in den geänderten Dissipationseigenschaften in der Relaxationszone liegt.

Contents

List of Abbreviations

ACC	Anomaly Correlation Coefficient
CGT	Circumglobal Teleconnection
CPPD	Caribbean-Pacific precipitation dipole
DJF	December, January, February
EASM	East Asian summer monsoon
ECMWF	European Centre for Medium-Range Weather Forecast
EOF	Empirical Orthogonal Functions
ENSO	El Niño-Southern Oscillation
gpdam	geopotential decameters
ISM	Indian summer monsoon
JJA	June, July, August
MCA	Maximum Covariance Analysis
NAE	North Atlantic-Europe(an)
NCAR	National Center for Atmospheric Research
NCEP	National Centers for Environmental Prediction
NOAA	National Oceanic and Atmospheric Administration
PC(A)	Principal Component (Analysis)
PCC	Pattern Correlation Coefficient
PNA	Pacific-North America pattern
PJ	Pacific-Japan pattern
RWS	Rossby wave source
SI	sea ice
SEA	Summer East Atlantic
slp	sea level pressure
SNAO	Summer North Atlantic Oscillation
SST	sea surface temperature
WPNA	Western Pacific-North America pattern
WNPSM	Western North Pacific summer monsoon

1 Introduction

Until recently, most analyses of climate variability in the North Atlantic/European (NAE) sector have focused on the winter season. Interest in the boreal summer variability has been growing due to the frequent occurrences of extreme summers with large socio-economic impacts from the beginning of the 21st century onward (Coumou and Rahmstorf, 2012). In western Europe, the exceptionally hot and dry summer of 2003 (Fink et al., 2004) caused great economic losses and many heat-related deaths (Schär and Jendritzky, 2004), while the heat wave of 2010 impacted eastern Europe and western Russia particularly severely (Lau and Kim, 2012). Many studies within this area of interest address the potential for predictability of extreme temperature and precipitation events and attempt to identify climatic factors relevant for their preconditioning (for the extreme summer of 2003 see e.g. Black et al., 2004; Weisheimer et al., 2011; for 2010 see Dole et al., 2011). For the winter season, extreme events are often connected to anomalously strong phases of the large-scale patterns of interannual variability that influence the jet stream such as the North Atlantic Oscillation (NAO, see e.g. Hurrell et al., 2003). Boreal summer low-frequency variability modes and their regional climate impacts have been less extensively studied, partly because the weather regimes in this season are not as clearly separable as in winter and appear to be less dominant (Hurrell and Deser, 2010).

Barnston and Livezey (1987) were among the first to systematically analyse the prevailing circulation patterns in the northern hemisphere in all seasons. They apply a rotated principal component analysis (RPCA) to monthly northern hemisphere 700 hPa geopotential height observations from 1950 to 1984 and find the NAO to be the only pattern that is prevalent in every month of the year noting that its structure has pronounced seasonal variability. In the NAE sector, the winter NAO is characterised by a meridional dipole with centres of action located over Iceland and the Azores. In its summer configuration the NAO is of weaker amplitude, smaller spatial extent, shifted northward, and has a northeast-to-southwest orientation. It is the only pattern with a clear signature in the NAE sector that they find for the summer season.

The term summer NAO (SNAO) was coined later by Folland et al. (2009) who offer a detailed description of this most dominant mode of summer variability in the NAE sector and its impacts on the regional surface climate. They define the SNAO as the first empirical orthogonal function (EOF) of July to August mean sea level pressure (slp) anomalies over the region from 25°N - 70°N and 70°W - 50°E where it explains 28.3% of the 2-month slp variance. Compared to the winter NAO, it is

of smaller spatial extent and located further north. Additionally, its southern centre of action is shifted eastward while the northern centre is weaker and shifted westward. Nevertheless, they find the SNAO to exert a significant control on the near surface temperature, cloudiness, and precipitation inside the region: summers under the influence of a positive SNAO tend to be dry, warm and relatively cloud-free in north-western Europe and more weakly so over north-east North America, while they are anomalously wet, cool and cloudy in south-eastern Europe. There is also evidence for a SNAO influence on Mediterranean precipitation (Bladé et al., 2012). Due to these impacts on the surface climate, it is conceivable that extreme events can be controlled by the predominance of either phase of the SNAO. Cassou et al. (2005) are able to show that the likelihood for extreme warm days in France is significantly enhanced during the positive phase of the SNAO. By cluster analysis they identify another summer weather regime that they name the Atlantic Low which is as prevalent during summer as both phases of the SNAO. This regime is also associated with a much higher chance for extremely hot days. Since there are potentially substantial impacts of the low-frequency summer variability on the surface climate, one main aim of this thesis is to clearly characterize and analyse the modes of variability in the NAE sector.

In light of the link between the large-scale circulation and surface summer climate, the question arises whether there is potential for predicting the summer circulation. Seasonal predictability can arise from slowly-evolving lower boundary forcing, and there is observational evidence that the summer atmosphere over the North Atlantic is locally forced by sea surface temperature (SST) anomalies that modify the turbulent air-sea heat fluxes (Gastineau and Frankignoul, 2015). A second premise for seasonal predictability is the existence of atmospheric teleconnection patterns that link low-frequency extratropical variability with variability outside of the mid-latitudes - most often in the tropics (Shukla et al., 2000).

In order to investigate the influence of lower boundary forcing, a seasonal ensemble forecast can be produced by prescribing observed SST and sea ice (SI) at the boundary of the atmospheric model. By ensemble averaging the signal forced by the anomalous boundary conditions can be isolated from the internal variability. Alternatively, the outcome could be compared to a control run that uses climatological SST and SI instead. As a means for studying remote influences on the atmospheric circulation in the mid-latitudes, a relaxation[1] technique is commonly used in seasonal hindcast experiments (see e.g. Jung et al., 2010a; Douville et al., 2011). In this approach, the forecast error of the model is artificially reduced by relaxing the model towards reanalysis data in a specified region (Jung et al., 2010a). This enables one to study the impact of an "improved" simulation in a certain region on the prediction in an area away from the relaxation zone. For example, Greatbatch et al. (2012) apply the technique to investigate remote influences on winter circulation anomalies in the northern hemisphere over the ERA-40 period and identify an influence of the

[1] Also referred to as nudging.

stratosphere on the NAO and a tropical control of the Pacific-North American (PNA) pattern. Single exceptional winters in Europe have also been shown to have a tropical origin by using a relaxation approach (Jung et al., 2010b; Greatbatch et al., 2015). This technique has thus far mostly been applied to study the northern hemisphere winter circulation but also offers a promising tool for investigating teleconnections in the summer season (Douville et al., 2011).

One reason for the small number of studies addressing summer teleconnections is that these are understood to be mostly associated with stationary planetary waves. These rely strongly on the presence of meridional potential vorticity gradients that are generally weaker in summer than in winter (Palmer and Anderson, 1994). Another factor is that the zone of tropical easterlies has a larger meridional extent, i.e. the zero wind line lies further north than in winter. Nonetheless, Ding and Wang (2005) find a circumglobal teleconnection pattern (CGT) in the summer northern hemisphere. The CGT is a zonally-oriented wave train of geopotential height anomalies of alternating signs circling the globe in a broad meridional band from the sub- to the extratropics. It is accompanied by anomalies in precipitation and temperature throughout the mid-latitudes. The authors further relate this pattern to diabatic heating anomalies associated with the Indian summer monsoon (ISM) and the El Niño-Southern Oscillation (ENSO). It can be shown by use of a linear barotropic model that this pattern is an internal mode of the northern hemisphere summer atmosphere but can also be forced by the ISM (Ding et al., 2011; Lin, 2009). A second teleconnection pattern is the so-called western Pacific-North America pattern (WPNA) which links rainfall of the western North Pacific summer monsoon (WNPSM) to circulation anomalies over the United States and also to weaker anomalies in the NAE sector (Ding et al., 2011). Neither of these patterns, however, has been shown to project onto the SNAO.

The tropical and extratropical atmosphere can in principle be linked through either a tropospheric or a stratospheric pathway. However, since this link involves the propagation of Rossby waves, the background flow field is important in determining the possibility of either route. Charney and Drazin (1961) show that it is not possible for planetary waves to propagate vertically in an easterly background flow; since the summer stratosphere is governed by easterly winds, a stratospheric pathway for a tropical-extratropical teleconnection is unlikely. The possibility of horizontal Rossby wave propagation through the troposphere also depends on the background flow (Hoskins and Ambrizzi, 1993). By using ray tracing arguments, Hoskins and Ambrizzi (1993) show that wave guides can exist where there is a local maximum in the meridional absolute vorticity gradient which is often connected to the position of the jet streams. Within these wave guides, planetary waves can propagate zonally over large distances and thus create teleconnection patterns. These wave guides exist in the winter northern hemisphere and are associated with circumglobal teleconnections (Branstator, 2002). However, in the tropics easterly winds prevail throughout

the year; thus Rossby wave propagation is suppressed. It is thus important to establish how a tropical signal can leave the tropics to excite a wave train in the extratropical atmosphere in the first place. The mechanism works as follows (Trenberth et al., 1998): convective activity in the tropics, perhaps related to positive SST anomalies, affects the large scale overturning of the Hadley circulation. The tropical upper tropospheric divergence associated with the heating is balanced by upper tropospheric convergence and subsidence in the descending branch of the Hadley Cell which is located in the subtropics, i.e. outside of the zone of easterlies. Here, the anomalous divergent component of the flow acts as a major Rossby wave source (RWS) which is relatively insensitive to the exact location of the convection region (Sardeshmukh and Hoskins, 1988). In fact, the diabatic forcing induced by convection is often related to the monsoon systems which can be located quite far north of the equator. Thus, the monsoons can be influential in exciting teleconnection patterns. If it is possible to establish such a link for the summer variability in the NAE sector, seasonal predictions could be improved significantly by a better representation of moist convection. In fact, Douville et al. (2011) show that the simulation of mid-latitude stationary waves with the Arpege-Climat atmospheric general circulation model in boreal summer benefits strongly when forecast error in the tropics is suppressed by relaxing the tropical atmosphere towards reanalysis data. They also point out that the impact of correctly representing subsidence in the equatorial tropical Pacific is even higher than that of improving the representation of the monsoons.

Few studies have focused on local and remote controls of the summer NAE variability. For example, Hall et al. (2016) apply a linear lead/lag regression approach to observational and reanalysis data to identify the dominant predictors of the North Atlantic polar jet stream speed and position. They find that Atlantic SST, sea ice (SI) in the Barents and Kara Seas, and solar variability are the most statistically relevant predictors for the jet stream metrics. The authors also address tropical rainfall but find its influence to be small despite the aforementioned physical connection. Another potentially important predictor of boreal summer variability in the NAE sector is the Atlantic Multidecadal Variability (AMV)[2], which is a basin-wide SST anomaly in the North Atlantic with a time scale of 65-70 years (Schlesinger and Ramankutty, 1994). Reanalysis data (Folland et al., 2009) and a coupled model that simulates the AMV as part of its internal variability (Knight et al., 2006) have shown an anti-correlation between the AMV and the SNAO on interdecadal time scales.

Efforts to find the dominant teleconnection patterns of the northern hemisphere have addressed the NAE sector marginally. On the other hand, some work has been done on the local and remote boundary forcing of NAE sector summer variability, but this has mainly focused on statistical relationships (Hall et al., 2016). Thus, the second goal of this thesis is to identify external controls on the summer circulation in the NAE sector and establish a physical mechanism for these links.

[2] Also referred to as the Atlantic Multidecadal Oscillation (AMO).

The thesis will be structured as follows: in chapter 2, we introduce the data used to study boreal summer climate variability and present the design of the seasonal hindcast experiments and the implementation of the relaxation technique. In the same chapter the analysis techniques that are applied to the data are described. Following this, we show the dominant modes of summer variability in the NAE sector and discuss their circulation patterns and possible local impacts on the surface climate in chapter 3. In chapter 4 we then move to the analysis of the relaxation experiments and elaborate on the results by further examining teleconnection mechanisms that appear likely in the context of the seasonal hindcasts. These mechanisms are critically discussed by comparing our results with previous studies. We end this thesis by summarising the main points of our study in chapter 5 and give a brief outlook for future work.

2 Data and methods

2.1 Data

2.1.1 Reanalysis data

In order to investigate the extratropical summer variability and its global teleconnections, we will utilize the European Centre for Medium-Range Weather Forecast (ECMWF) Reanalysis ERA-Interim (Dee et al., 2011). ERA-Interim is a global atmospheric reanalysis that extends back to 1979 and is updated continuously until present. This reanalysis is produced by the ECMWF Integrated Forecast System (IFS) which is run at a horizontal T255 spectral resolution (corresponding to approximately 0.71° or 79km at the equator) with 60 hybrid sigma-pressure vertical levels up to 0.1 hPa and a time step of 30 minutes.

The data has been downloaded from the ECMWF web page as 6-hourly fields at the analysis time step for the years from 1980-2014 interpolated to a 2.5° x 2.5° regular grid.

The reanalysis data will in the following be treated as the best approximation of the true state of the atmosphere and will thus sometimes be referred to as the observations. We want to stress however, that the reanalysis data is of course not a purely observational product but output from a model that assimilates observations. Hence, the data is also subject to model errors.

2.1.2 Precipitation data

Even though there are no reported issues with precipitation in ERA-Interim, especially tropical rainfall can be a problem due to errors in the parametrization of moist convection. To avoid these problems, we use a quasi-observed precipitation product from the Climate Prediction Center Merged Analysis of Precipitation (CMAP) (Xie and Arkin, 1997). To generate the global, gridded (2.5°x2.5°) CMAP dataset, rain gauge data and satellite measurements are combined with reanalysis data from the National Centers for Environmental Prediction-National Center for Atmospheric Research (NCEP-NCAR). The CMAP data is available from 1979 onwards and is continuously updated until present. It should be noted that a varying number of observations enter the grid box estimates of precipitation and especially at high latitudes, where observations are sparse, there are issues with these precipitation estimates. Furthermore, the number of observations - and thus the quality of the data - does

not only differ spatially but also temporally. For instance, microwave satellite measurements are only reliable from 1987 onwards (Xie and Arkin, 1997). Before that, the estimates rely on rain-gauge data and the reanalysis only. However, the CMAP data has been reported to reliably represent the large-scale precipitation patterns and its temporal evolution (Yin et al., 2004) and will therefore be used in the following.

2.1.3 Experimental set-up

To investigate the effect of atmospheric teleconnections on the seasonal prediction skill, we perform a suite of different seasonal hindcasts. These are generated with the ECMWF IFS (cycle 40r1) that is used to produce ERA-Interim (see 2.1.1). To obtain a single hindcast for the boreal summer season the model is initialized around May 1, 00 UTC each year (1980-2014) from the atmospheric state at the initialisation time given by ERA-Interim and calculated forward for 120 days (i.e. until the end of August). Since the model simulates the atmosphere only, we need to prescribe sea surface temperature and sea-ice (SST/SI) at the lower boundary which is done using ERA-Interim SST/SI. In order to be able to separate internal from external variability, 9 single hindcasts are performed to generate an ensemble, each initialized 6 hours later than the previous one (i.e. May 1, 00UTC $+ n \cdot 6h$, for $n = 0, 1, 2, ..., 8$). This ensemble size should be sufficient to separate internal, given by the spread of the ensemble members, from external variability, given by the ensemble average (Hansen et al., 2017).

The relaxation technique

The general idea of a relaxation experiment is to ensure that the used model is close to the observed atmospheric state in a specified region over the entire course of the simulation. The aim of this is then to identify what influence this 'perfect prediction' has on the prediction in other parts remote from the relaxation region.

How is perfect predictability sought? At each time step the model is 'pulled' toward the observed climate by relaxing a suite of atmospheric variables using the following formulation added to the model prognostic equation of the relaxed variables:

$$\frac{d\underline{\mathrm{x}}}{dt} = \ldots + \lambda(\underline{\mathrm{x}} - \underline{\mathrm{x}}^{\mathrm{ref}}) \tag{2.1}$$

where $\underline{\mathrm{x}}$ is the model state vector that consist of the fields of all relaxed variables and $\underline{\mathrm{x}}^{\mathrm{ref}}$ is the observed state vector, in this case given by the 6-hourly ERA-Interim output linearly interpolated in time. Here, zonal and meridional velocity u and v, as well as temperature T and the logarithm of surface pressure $\ln p_s$ are relaxed. In this way the model error is synthetically reduced. The magnitude of this reduction is specified through the relaxation parameter λ which is given as an inverse time scale. A value of $\lambda = 0.1(\text{time step})^{-1}$ would indicate that the model is corrected by 10%

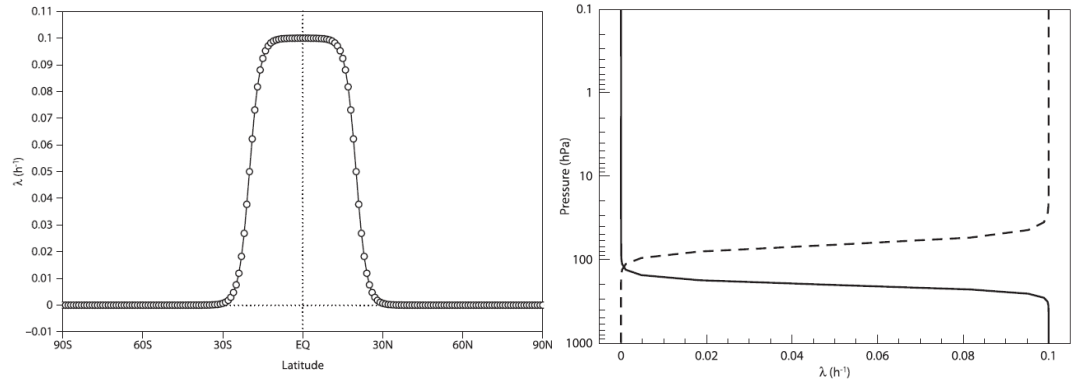

FIGURE 2.1: Figure 1 and 2 from Jung et al. (2010a). Left: latitudinal profile of the relaxation parameter λ in h^{-1} for an experiment with tropical relaxation. Right: vertical profile of λ in h^{-1} for an experiment with relaxation in the troposphere (solid) and the stratosphere (dashed). Note that in both panels, values on the λ axis must be doubled to be applicable to our experiments.

of the model error at each time step. For a model time step of 30 minutes this results in a relaxation time scale of 5 h. The relaxation parameter is a function of space allowing for a limitation of the relaxation to certain parts of the atmosphere (e.g. the tropics or the stratosphere). Since the correction is not physical and might not be consistent with the model's climate, it is important to have a smooth transition from a relaxation to a non-relaxation region. This supposed to to reduce spurious reflection and dissipation of atmospheric waves in the transition zones although these cannot be eliminated entirely. In the horizontal, λ follows a hyperbolic tangent, decreasing from a value $\lambda_0 = \frac{1}{5}h^{-1}$ in the relaxation region to 0 within 20° of latitude. This is illustrated for tropical relaxation in Fig. 2.1a (taken from Jung et al., 2010a). In the vertical this transition zone extends over approximately 13 model levels. This is shown for relaxation in the troposphere and the stratosphere in Fig. 2.1b (also from Jung et al., 2010a).

Relaxation experiments

Since we want to test for remote influences from different parts of the climate system on the prediction of the extratropical seasonal circulation we apply the aforementioned relaxation technique in a variety of regions. These are only confined meridionally but extend over all longitudes. The exact set-ups of the experiments (each an ensemble of 9 members) and their names are listed in Table 2.1. The first part of the experiment name specifies whether the boundary conditions for the atmospheric model are daily climatological means of SST/SI (CLIM) or observed SST/SI anomalies (OBS). This enables us to also identify forcings that arise due to the boundary conditions. The second part of the experiment name specifies the relaxation region. In CLIM-NO for example, the model is run freely with neither relaxation nor anomalous boundary forcing. Thus, in this ensemble, not only the ensemble spread but also the year-to-year variability arises from the varying initial conditions alone. OBS-NO

TABLE 2.1: List of all relaxation experiments used in this study. Boundaries of the relaxation regions refer to the latitude/height where $\lambda = 0.5\lambda_0$, i.e. the centre of the profile of λ as discussed in the text.

Experiment	**Relaxation Region, meridional**	**Relaxation Region, vertical**	**SST/SI**
CLIM-ARC	Arctic (75°N-90°N)	troposphere approx. 320 hPa - surface (model levels 34-60)	climatological
CLIM-NO	None	None	climatological
CLIM-STRA-NH	northern hemisphere (30°N-90°N)	stratosphere approx. 0.1 - 55 hPa (model levels 1-22)	climatological
CLIM-TROPICS	tropics (20°S-20°N)	full atmosphere	climatological
OBS-NO	None	None	observed
OBS-TROPICS	tropics (20°S-20°N)	full atmosphere	observed

on the other hand should produce a response to the yearly varying observed boundary forcing of global SST/SI. In this regard it is also important to note that the difference between CLIM-TROPICS and OBS-TROPICS lies almost exclusively in the specification of extratropical SST/SI in the latter. Prescribing lower boundary conditions within the relaxation region (in this case the tropics) has little effect on the relaxed atmosphere. Additionally, the relaxation itself should already contain the signal of varying SST.

2.2 Methods

2.2.1 Linear regression

For the purpose of estimating the linear response of a variable $\boldsymbol{Y}$ to changes in a variable $\boldsymbol{X}$ (i.e. the regression of $\boldsymbol{Y}$ onto $\boldsymbol{X}$) we formulate a regression model. With $(x_1, y_1), ..., (x_n, y_n)$ as pairs of data of $\boldsymbol{X}$ and $\boldsymbol{Y}$, we define a linear model as:

$$y_i = \beta_0 + \beta_1 x_i + \eta_i, \quad i = 1, 2, \ldots, n$$

where η_i are the residuals that are not captured by the linear model. The parameters β_0 and β_1 of the model are estimated by minimizing the sum of squared deviations:

$$SS = \sum_{i=1}^{n} (y_i - \beta_0 - \beta_1 x_i)^2$$

which can be done by setting the first order partial derivatives of SS with respect to β_0 and β_1 to zero.

In the case where $\boldsymbol{X}$ refers to time, β_1 will be called the linear trend.

Removal of a signal

If there is a dominant signal in the data that we are not interested in describing or relating to other variables, we will remove it applying the above formulated linear model. In that case, the signal will be $\boldsymbol{X}$ and the "signal-removed" anomalies will be simply the corresponding residuals $\boldsymbol{\eta}$. Thus, when e.g. $\boldsymbol{X}$ is time, $\boldsymbol{\eta}$ is the detrended data.

2.2.2 Correlation

In order to evaluate how well the model anomalies $\boldsymbol{Y}$ of a variable reproduce the time evolution of the observed anomalies $\boldsymbol{X}$, we estimate an anomaly correlation coefficient (ACC) as:

$$\mathrm{ACC} = \frac{\sum_{i=1}^{n} X_i Y_i}{\sqrt{\sum_{i=1}^{n} X_i^2 \sum_{i=1}^{n} Y_i^2}} \tag{2.2}$$

where the index i refers to time. Unless stated otherwise, $\boldsymbol{X}$ and $\boldsymbol{Y}$ are detrended variables.

2.2.3 Pattern correlations

As a primitive measure of how alike two patterns $\boldsymbol{S}$ and $\boldsymbol{T}$ are that only have a spatial dimension of length l, we estimate a pattern correlation coefficient (PCC). It is defined as follows:

$$\mathrm{PCC} = \frac{\widehat{\mathrm{Cov}}^{\mathrm{w}}(S,T)}{\sqrt{\widehat{\mathrm{Cov}}^{\mathrm{w}}(S,S)\widehat{\mathrm{Cov}}^{\mathrm{w}}(T,T)}} \tag{2.3}$$

with $\widehat{\mathrm{Cov}}^{\mathrm{w}}(S,T)$ the weighted covariance of $\boldsymbol{S}$ and $\boldsymbol{T}$:

$$\widehat{\mathrm{Cov}}^{\mathrm{w}}(S,T) = \frac{\sum_{j=1}^{l}(S_j - \bar{S}^{\mathrm{w}})(T_j - \bar{T}^{\mathrm{w}})W_j}{\sum_{j=1}^{l} W_j} \tag{2.4}$$

where the index j refers to the grid point and the W_j are the elements of the weighting vector $\boldsymbol{W}$ that is given by the cosine of latitude for each grid point j. The $\bar{S}^{\mathrm{w}}$ and $\bar{T}^{\mathrm{w}}$ are the weighted means of $\boldsymbol{S}$ and $\boldsymbol{T}$ respectively:

$$\bar{S}^{\mathrm{w}} = \frac{\sum_{j=1}^{l} S_j W_j}{\sum_{j=1}^{l} W_j} \tag{2.5}$$

2.2.4 Significance testing

Correlations and regression coefficients are considered statistically significant if they are significantly different from 0 on the 95% level based on a Student's t-test with degrees of freedom equal to the sample size minus 2. This is only valid if the single time steps are independent of each other. This criterion is probably met to a fair

degree when we consider seasonal means but it must be kept in mind that the time series could be serially correlated.

Due to the large spatial auto-correlation of the fields of all climate variables considered here, we do not provide significance thresholds when we consider pattern correlations.

2.2.5 Principal Component Analysis/Empirical Orthogonal Functions

Seeking to identify the dominant patterns of low-frequency variability in the extratropical atmosphere, we apply a Principal Component Analysis (PCA). This multivariate technique has been widely used in climate science since it was first introduced to the field by Lorenz (1956). We want to discuss briefly its purpose, theoretical basis, application and some limitations. For an elaborate review of the method, the reader is referred to von Storch and Zwiers (1999, chapter 13) and von Storch and Navarra (1995, chapter 13).

In climate science one is often confronted with data of high dimensionality. Thus, multivariate statistical techniques are needed that allow one to separate the part of the variability that one is interested in (the signal) from the noise. Put differently, one wants to describe the main part of the variability of a dataset by only a few patterns or modes.

Following the notation by in chapter 13 of von Storch and Navarra (1995) we assume an m-variate random vector $\vec{\boldsymbol{X}}$ with first moment $\mathrm{E}[\vec{\boldsymbol{X}}] = 0$. We now want to split the data into a signal part and a noise part by writing $\vec{\boldsymbol{X}}$ as:

$$\vec{\boldsymbol{X}}_t = \sum_{k=1}^{K} \alpha_k(t)\vec{p}^{\,k} + \vec{n}_t \tag{2.6}$$

where the $K \leq m$ "guess patterns" $\vec{p}^{\,k}$ and their expansion coefficients $\alpha_k(t)$ describe the signal and $\vec{n}_t$ the noise subspace. Once we have determined the patterns $\vec{p}^{\,k}$, we are able to derive the expansion coefficients by projecting the data $\vec{\boldsymbol{X}}$ onto the adjoint patterns $\vec{p}_A^{\,k}$ (for derivation, see von Storch and Navarra, 1995):

$$\alpha_k = \langle \vec{p}_A^{\,k}, \vec{\boldsymbol{X}} \rangle \tag{2.7}$$

where $\langle , \rangle$ is the dot product.

In order to define the patterns, we need to formulate a condition that they need to fulfil. In EOF analysis, we are interested in minimizing the variance of the noise $\vec{n}$ under the constraint that all vectors $\vec{p}^{\,k}$ are orthogonal to each other, i.e. $\langle \vec{p}^{\,k^T}, \vec{p}^{\,i} \rangle = \delta_{ik}$ in which case the patterns are referred to as Empirical Orthogonal Functions (EOFs). Thus, we are seeking those vectors that minimize the variance of the residual:

$$\epsilon_K = \mathrm{E}\left[\left(\vec{\boldsymbol{X}} - \sum_{k=1}^{K} \alpha_k \vec{p}^{\,k} \right)^2 \right] \tag{2.8}$$

where $\alpha_k = \langle \vec{\boldsymbol{X}}^T, \vec{p}^k \rangle$ (from Eq. 2.7 under the condition that vectors $\vec{p}^k$ are orthogonal) are called the Principal Components (PC). With this, eq. 2.8 can be reformulated to:

$$\epsilon_K = \text{VAR}\left(\vec{\boldsymbol{X}}\right) - \sum_{k=1}^{K} \lambda_k \tag{2.9}$$

where λ_k are the eigenvalues of the covariance matrix $\boldsymbol{\Sigma} = \text{E}[\vec{\boldsymbol{X}}\vec{\boldsymbol{X}}^T]$. Due to the properties of the covariance matrix, the λ_k are positive. The eigenvectors of the covariance matrix are exactly the EOFs (von Storch and Navarra, 1995). The first K EOFs are constructed such that they capture a maximum of variance of $\vec{\boldsymbol{X}}$ in a minimum number of patterns.

In this thesis, we are mostly concerned with globally gridded data of length 35 years. In the majority of cases, we will deal with seasonal anomalies on a 2.5° by 2.5° grid, i.e. our random variable $\vec{\boldsymbol{X}}$ has (spatial) dimension $m = \frac{360 \cdot 180}{2.5^2} = 10,368$ and we have a finite number $n = 35$ of realizations, i.e. $\vec{\boldsymbol{X}} = \{\vec{x}(1), ..., \vec{x}(35)\}$. Prior to performing PCA, any linear trend (see 2.2.1) in time is subtracted from the data at each grid point, thus $\vec{\boldsymbol{X}}$ is the matrix of detrended anomalies. Furthermore, we multiply the data at each grid point by the square root of the cosine of latitude to weigh its variance by area. We can now estimate the covariance matrix $\hat{\boldsymbol{\Sigma}}$:

$$\hat{\boldsymbol{\Sigma}} = \frac{1}{n} \sum_{l=1}^{n} \vec{x}(l)\vec{x}(l)^T \tag{2.10}$$

of which we seek the eigenvectors $\hat{\vec{p}}^k$ (our estimated EOFs), eigenvalues $\hat{\lambda}_k$ and the coefficients $\hat{\alpha}_k(l) = \sum_{j=1}^{n} \vec{x}(l)_j \hat{p}_l^k$ which are the estimated PCs. We scale the EOFs such that they have the same units as $\vec{\boldsymbol{X}}$, while the PCs are dimensionless and have variance one.

We will only be concerned with the first few EOFs that explain the largest fraction of the variance of the data. The fraction of variance explained by the EOF $\hat{\vec{p}}^i$ is:

$$\hat{\gamma}_i = \frac{\hat{\lambda}_i}{\sum_{k=1}^{m} \hat{\lambda}_k}$$

This raises the question how many EOFs we should consider. North et al. (1982) show that the sampling error of an eigenvalue λ_k is approximated by:

$$\Delta\lambda_k \approx \sqrt{\frac{2}{n}}\lambda_k$$

with n the number of independent samples. They point out that if the spacing between two neighbouring eigenvalues is comparable in magnitude to $\Delta\lambda_k$ the sampling error of the EOF is similar in magnitude to the EOF associated with the neighbouring eigenvalue. This rule-of-thumb will serve as an indicator of whether an EOF is well separated from the next higher one. It should be noted at this point that on top of being just an approximation of the error, we are likely to underestimate the

error by using the total number of time steps for n. Even when considering seasonal anomalies, the assumption of independence of the realizations (i.e. the time steps) is not entirely valid.

At this point, another important constraint of the technique should be stressed. When using PCA in an attempt to separate modes of variability, the condition of the EOFs being orthogonal to each other is a purely statistical one and is not based on physical considerations. A comprehensive example of how this condition affects the patterns and their interpretation is illustrated in Dommenget and Latif (2002).

Naming conventions

To avoid confusion about the terminology when discussing the results in the following sections, we introduce some naming conventions here:

1. When we are concerned with **anomalies** these will be deviations from the seasonal climatological mean of the same dataset. We thus neglect any bias in the climatology but note that it is small in all cases.

2. To define the patterns of variability, we apply the PCA as described above to the reanalysis data. The resulting EOF1/EOF2 will be called the **observed SNAO/SEA pattern**.

3. The projection $\hat{\alpha}_{i_u}$ of *un*detrended anomalies $\vec{\boldsymbol{X}}_u$ onto the observed SNAO/SEA pattern ($\hat{\vec{p}}^i$) computed from detrended ERA-Interim anomalies $\vec{\boldsymbol{X}}$ will be referred to as the **SNAO/SEA index**, i.e:

$$\hat{\alpha}_{i_u} = \vec{\boldsymbol{X}}_u^T \hat{\vec{p}}^i, \quad i = \{1, 2\} \tag{2.11}$$

   This allows us to recover a trend towards the positive or negative phase of the EOFs. If the index time series is detrended (equivalent to projecting the detrended anomalies onto the observed SNAO/SEA), this will be explicitly pointed out.

   - If $\vec{\boldsymbol{X}}$ and $\vec{\boldsymbol{X}}_u$ are ERA-Interim data, we will refer to their projections onto the observed SNAO/SEA patterns as the **observed SNAO/SEA indices**.
   - The projection of undetrended *model* anomalies onto the observed SNAO/SEA will be called the **projected SNAO/SEA index**.

4. The sign of the EOFs and PCs is arbitrary as long as it fulfils eq. 2.11. The patterns/EOFs that are displayed in this thesis will always be referred to as the **positive phase** of the respective pattern.

2.2.6 Monte Carlo methods

When analysing the relaxation experiments in terms of possible forcings from the relaxation regions, we will apply a Monte Carlo method as in Greatbatch et al. (2012). Consider a time series that has been simulated by the 9 model ensemble members. At every time step, the realization simulated by any of the members should ideally be as likely as that of a different member. We can thus generate a new realistic (within the context of the model) time series by randomly selecting one out of the 9 possible values from each summer. That way, we can generate a sample of much larger size than the ensemble. In our analysis we choose a number of 10,000 repetitions of this random selection process.

We can now compute the correlation between all these realizations and the observed time series, leaving us with a distribution of 10,000 correlation coefficients. If the correlation histogram is centred around 0, we can conclude that there is no predictive skill in this relaxation experiment. If the distribution is shifted towards positive values, it is more likely that there is a forcing from the relaxation region. When the distribution is shifted so strongly that correlations of 0 become rare, our confidence in the importance of the forcing is high.

The same Monte Carlo technique can be applied to study how likely a certain trend is under the forcing from the relaxation region. We can generate a distribution of trends that are possible within the context of a certain relaxation experiment. Depending on where the observed trend lies within this distribution, we can judge how likely it would be under the considered forcing.

2.2.7 Derived variables

In the following, two variables are briefly introduced. These are not part of the ERA-Interim or model output fields but must be calculated. To reduce biases in the seasonal means, we follow the suggestions of Shimizu and de Albuquerque Cavalcanti (2011) and compute these variables from daily wind fields and then average seasonally.

Rossby wave source

The Rossby wave source (RWS) was first introduced by Sardeshmukh and Hoskins (1988). Using their notation, at an upper tropospheric level, the non-linear vorticity equation may be written as:

$$\left(\frac{\partial}{\partial t} + \boldsymbol{v} \cdot \boldsymbol{\nabla}\right) \zeta = -\zeta \boldsymbol{\nabla} \cdot \boldsymbol{v} + F \tag{2.12}$$

where $\boldsymbol{v}$ is the horizontal flow field, ζ the absolute vorticity and F a frictional forcing term. Based on the Helmholtz decomposition of any vector field $\boldsymbol{F}$ into the sum of a curl-free and a divergence-free vector field as $\boldsymbol{F} = -\boldsymbol{\nabla}\Phi + \boldsymbol{\nabla} \times \boldsymbol{A}$ (where Φ is a scalar

potential and $\boldsymbol{A}$ a vector potential), we are able to split the flow into its rotational ($\boldsymbol{v_\psi}$) and divergent ($\boldsymbol{v_\chi}$) components:

$$\boldsymbol{v} = \boldsymbol{\nabla}\chi + \boldsymbol{k} \times \boldsymbol{\nabla}\psi = \boldsymbol{v_\chi} + \boldsymbol{v_\psi}$$

where χ is the velocity potential, ψ the streamfunction and $\boldsymbol{k}$ the unit vector in z-direction. We can thus rewrite eq. 2.12 as:

$$\left(\frac{\partial}{\partial t} + \boldsymbol{v_\psi} \cdot \boldsymbol{\nabla}\right)\zeta = S + F \tag{2.13}$$

where S is the RWS given by:

$$S = -\boldsymbol{\nabla} \cdot (\boldsymbol{v_\chi}\zeta) = -\boldsymbol{v_\chi} \cdot \boldsymbol{\nabla}\zeta - \zeta\boldsymbol{\nabla} \cdot \boldsymbol{v_\chi} \tag{2.14}$$

From this, it follows that a source of positive vorticity (i.e. $S > 0$) in a certain place in the upper troposphere is due to the combined effect of advection of vorticity out of that area by the divergent component of the flow ($\boldsymbol{v_\chi} \cdot \boldsymbol{\nabla}\zeta < 0$) and vortex stretching caused by convergence of the flow ($\zeta\boldsymbol{\nabla} \cdot \boldsymbol{v_\chi} < 0$).

Stationary wave number

In order to analyse the possibility for the existence of stationary, planetary waves in the troposphere, we will make use of a measure that was first introduced by Hoskins and Ambrizzi (1993). This is the stationary wave number K_S which is derived from the dispersion relation for barotropic, stationary Rossby waves in background zonal flow U:

$$K_S = \sqrt{\frac{\beta - U_{yy}}{U}} \tag{2.15}$$

where $\beta = \frac{\partial f}{\partial y}$ is the meridional gradient of planetary vorticity f and $U_{yy} = \frac{\partial^2 U}{\partial y^2}$ the second derivative of the zonal wind U.

Following Hoskins and Ambrizzi (1993), this number can be interpreted as follows: where it is real, propagation of Rossby waves with zonal wave number $k^2 < K_S^2$ is supported by the background flow. These waves will be refracted away from the turning latitudes where k^2 approaches K_S^2 into regions of higher K_S but will break in the critical layers where $K_S \to \infty$. This implies that especially localized, finite maxima of K_S are vital since these act as guides for the Rossby waves.

Reflecting layers occur where $K_S \to 0$. In these, stationary waves are evanescent since no Rossby wave can propagate into them. This situation occurs where either the meridional planetary vorticity gradient β becomes weak, the background flow U large or where the meridional curvature of the background flow U_{yy} is large. On the other hand, K_S becomes large where $U \to 0$, i.e. in regions where the background flow changes from westerly to easterly. Thus, the position of the zero wind line (where $U = 0$) is important in determining where the critical layers are located.

3 Observed boreal summer variability in the North Atlantic-European sector

Since boreal summer variability in the NAE sector has attained much less attention than its winter counterpart, we want to focus on the main dynamics of the large-scale boreal summer circulation in some detail here. To get an estimate of the dominant modes of variability, we applied a PCA to JJA seasonally averaged geopotential height anomalies at 500 hPa (z_{500}) for the period from 1980 to 2014 from ERA-Interim over the area from 40°N to 70°N and 90°W to 30°E (hereafter used equivalently with the term NAE sector/region) as in Greatbatch and Rong (2006). In the following, we will discuss the two dominant EOFs since only these can be considered well separated from the higher modes (Fig. A.1); together they explain more than 50% of the seasonally averaged boreal summer variance in z_{500}.

3.1 Dominant mode of summer variability - the summer North Atlantic Oscillation

Circulation pattern

The observed EOF1 of JJA z_{500} anomalies is displayed in Fig. 3.1 and accounts for about 36% of boreal summer variance in the NAE sector. The amount of variance explained is of similar magnitude as that of the winter NAO (Hurrell et al., 2003). Despite the use of a different data product, z_{500} instead of slp and a different area over which the PCA has been applied, the pattern bears close resemblance to the summer NAO (SNAO) as described e.g. by Folland et al. (2009). Due to this similarity, the EOF1 of ERA-Interim z_{500} anomalies will in the following be referred to as the observed SNAO and its associated PC1 as the observed SNAO index.

Like its winter counterpart, two main centres of action constitute the SNAO pattern. The stronger of the two centres is located slightly west of the British Isles with geopotential height anomalies of up to 2.4 geopotential decameters (gpdam) associated with one standard deviation in the SNAO index. The weaker node lies west of the southern part of Greenland (anomalies up to 1.8 gpdam). The main height gradient is thus oriented north-westward which shows that the SNAO corresponds to anomalies in both the zonal and the meridional components of the geostrophic

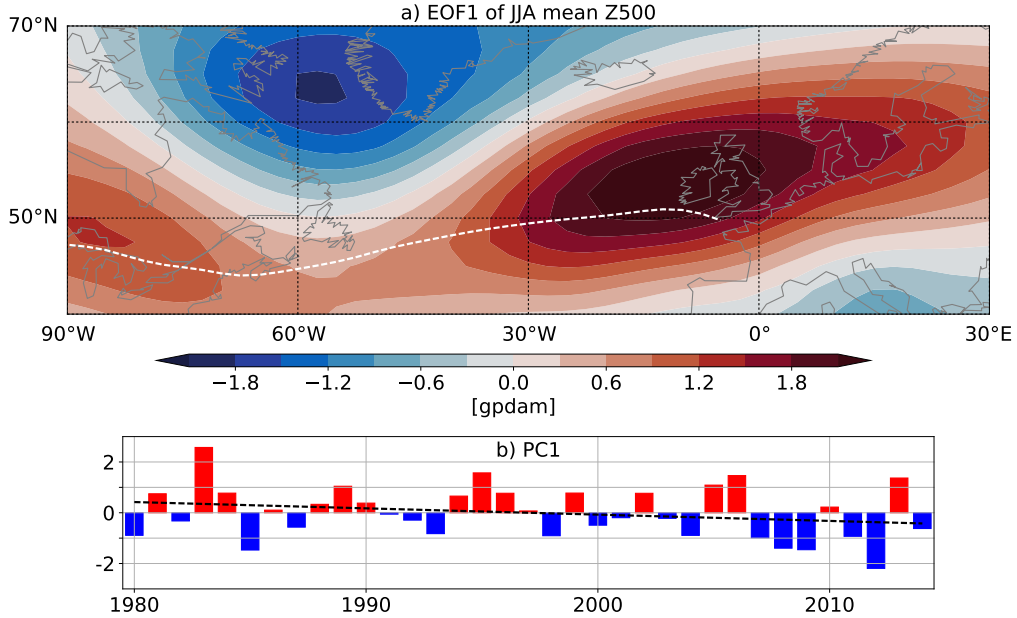

FIGURE 3.1: (a) The observed SNAO pattern defined as the first EOF of JJA mean ERA-Interim z_{500} anomalies over the NAE region (40°N - 70°N, 90°W - 30°E) and (b) observed SNAO index time series (bars) and its linear trend (black dashed line). White dashed line in the top panel indicates the position of the meridional maximum of JJA mean wind speed at 500 hPa in the Northern Hemisphere as an approximation for the position of the jet stream. The pattern shown is defined as the positive phase. EOF1 explains 36% of the boreal summer z_{500} variance.

wind. In the positive SNAO phase, the jet stream is redirected northward over eastern North America, the North Atlantic and Europe (Fig. A.2) and involves a significant meridional component and meandering. This is in contrast to the winter NAO whose positive phase corresponds to a more zonal jet stream. In the negative SNAO phase, the geostrophic wind anomalies that follow from the height field suggest a more southward position of the jet in the eastern part of the sector.

We examine the vertical structure of the SNAO by regressing slp and z_{200} onto its index. The centres of action at the surface are shifted eastward compared to those at 200 hPa but in general the regression patterns are highly similar at the surface and in the upper troposphere over the entire NAE region (Fig. A.3). This suggests that the SNAO is an equivalent barotropic phenomenon.

The time series of the SNAO index (Fig. 3.1b) has a tendency towards the negative phase (trend: -0.25 (decade)$^{-1}$). This trend however, is not significantly different from 0.

Relation to other climate variables

We now want to turn our attention to how other climate variables covary with the SNAO circulation. When temperatures at 850 hPa (T_{850}) are regressed onto the SNAO index, strong positive and negative temperature anomalies of up to 0.9 K

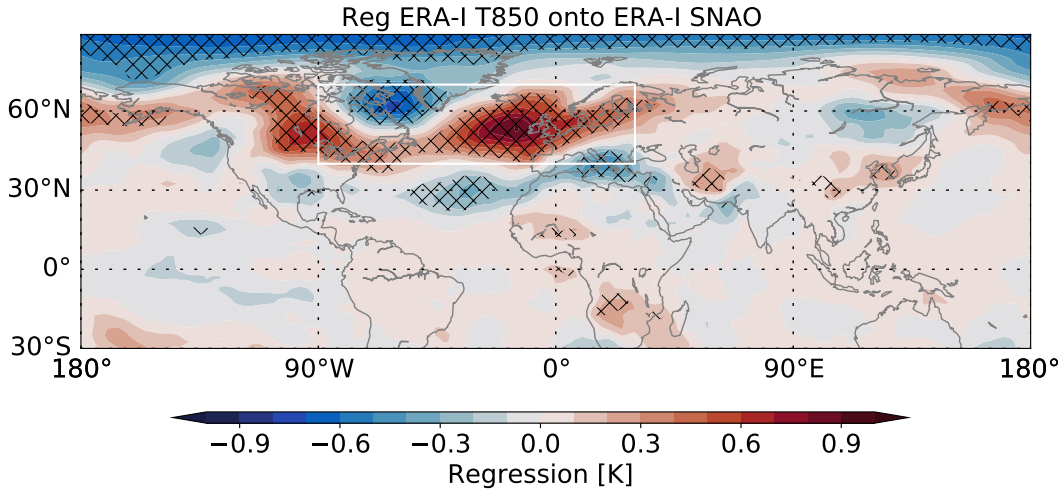

FIGURE 3.2: Regression of detrended ERA-Interim JJA mean temperature anomalies at 850 hPa onto the detrended observed SNAO index (shading). Units are K per one standard deviation of the SNAO index. Hatching shows regression coefficients that are statistically significant at the 95% level based on a t-test. White box indicates the area that the PCA was performed over.

arise over the NAE sector and partially beyond its limits (Fig. 3.2). In the positive SNAO phase, higher than normal temperatures are observed in a broad band extending from the northernmost part of central Canada to the east coast of the American continent and further over the North Atlantic broadening towards Europe and decreasing in magnitude towards north-eastern Scandinavia. The positive SNAO is also related to below-average temperatures over the Labrador Sea, the subtropical North Atlantic and the Mediterranean. The regression pattern bears much resemblance to the SNAO pattern itself with strongest positive/negative temperature anomalies located in the anticyclonic/cyclonic centres of the SNAO. Even away from the direct neighbourhood of the NAE sector, some significant correlations[1] can be found. Throughout the Arctic, below average temperatures occur during the positive phase of the SNAO while temperature anomalies in the Bering Sea are positive. There are other areas with significant regression slopes but these are small in extent and due to the large spatial autocorrelation of the temperature field our confidence in their significance is low.

SST deviations from the JJA climatology (Fig. 3.3) regressed onto the observed SNAO exhibit a pattern in the NAE sector that is very similar to the regression maps of T_{850}. The temperature tripole, with negative anomalies south of Greenland followed by positive anomalies in the eastward extension of the Gulf Stream region and again lower than normal SST in the subtropical North Atlantic, is organized in narrower bands with smaller temperature deviations than when considering T_{850}. Within this pattern, maximum SST anomalies in the North Atlantic are up to 0.4 K

[1]Note that the regression coefficient shown in all regression figures is just the correlation scaled by the standard deviation of the variable that is regressed onto the PC since the PC itself is normalized to have standard deviation 1. Regions where the regression coefficient is significant are identical to areas where correlations between the PC and the variable are significant.

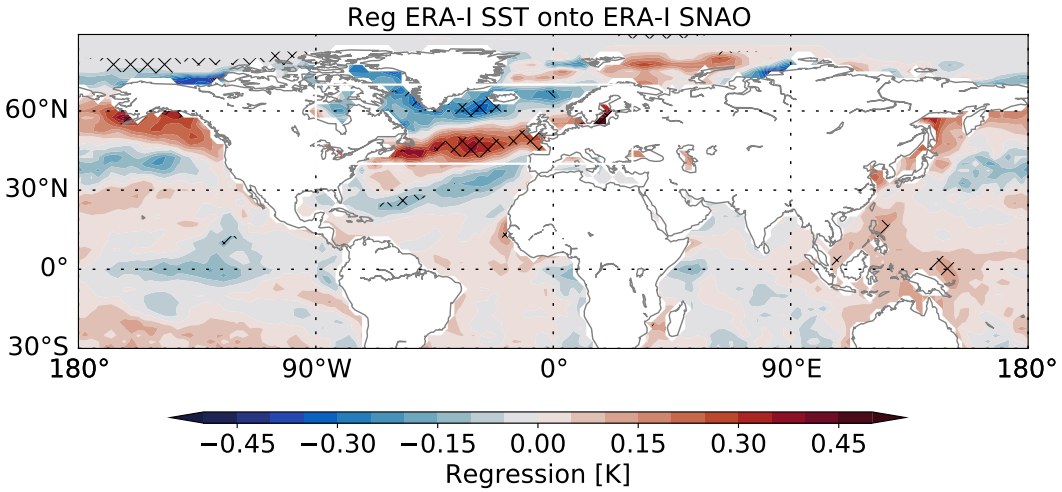

FIGURE 3.3: As in Fig. 3.2 but for SST regressed onto the SNAO index.

for one standard deviation of the SNAO index but the strongest deviations are observed in the Baltic Sea and are as large as 0.5 K. Outside of the domain however, SST does not covary strongly with the SNAO except in rather small areas in the Bering and Beaufort Seas and the Gulf of Alaska. The SNAO does not appear to be associated with anomalies in tropical SST on interannual time scales.

When regressing precipitation (Fig. 3.4) onto the SNAO index, a tripole pattern with south-eastern to north-western orientation similar to the one in T_{850} arises with above normal precipitation in the Mediterranean, anomalously dry conditions over Scandinavia, north western Europe, the British Isles and the eastern North Atlantic and again anomalously wet conditions over the Norwegian Sea over the north-western North Atlantic to the Labrador Sea. Moving away from the NAE region we

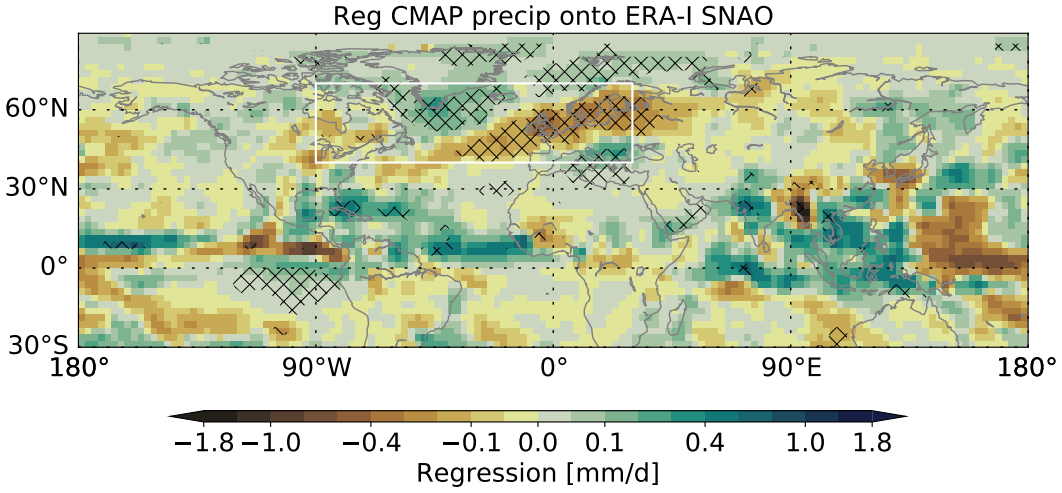

FIGURE 3.4: Regression of detrended CMAP precipitation onto the detrended observed SNAO index. Units are mm/d per one standard deviation of the SNAO index. Hatching indicates statistically significant regression coefficients. The white box marks the NAE region. Note the non-linear colour scale. Colours between colour map labels are linearly spaced (e.g. 3 levels between 0.1 and 0.4, i.e. spacing is 0.1).

find an area in the tropical east Pacific south of the Equator where small but significant positive deviations in precipitation arise together with positive SNAO index values. The same is true over the southern part of the Arabian peninsula. In the Caribbean, stronger wet anomalies are observed but these are not significant over a large area. This is also the case for a number of areas over the Maritime Continent. It is apparent that the largest SNAO related precipitation anomalies arise in the tropics but most of these are not statistically significant. This is due to the much larger variability of tropical precipitation. It can also be seen that there are no areas outside of the NAE sector where significant regressions in SST and precipitation arise in the same place.

3.2 Second dominant mode - the summer East Atlantic pattern

Circulation pattern

The second EOF is displayed in Fig. 3.5 and explains about 18% of JJA z_{500} variance in the NAE sector. It exhibits only one major centre of action located over the north-eastern Atlantic that extends north-westward over Greenland with anomalies up to 1.9 gpdam associated with one standard deviation in the time series. Two much weaker centres of opposite sign are found over the Baltic Sea and north-eastern Europe as well as over the western part of the North Atlantic right at the edge of the NAE region. While the zonal component of EOF2 is weak it has a distinct meridional component evident in the regression of meridional wind speed at 200 hPa (v_{200}) onto the PC2 time series (Fig. 3.6). Clearly, the PC2 is associated with significant north-

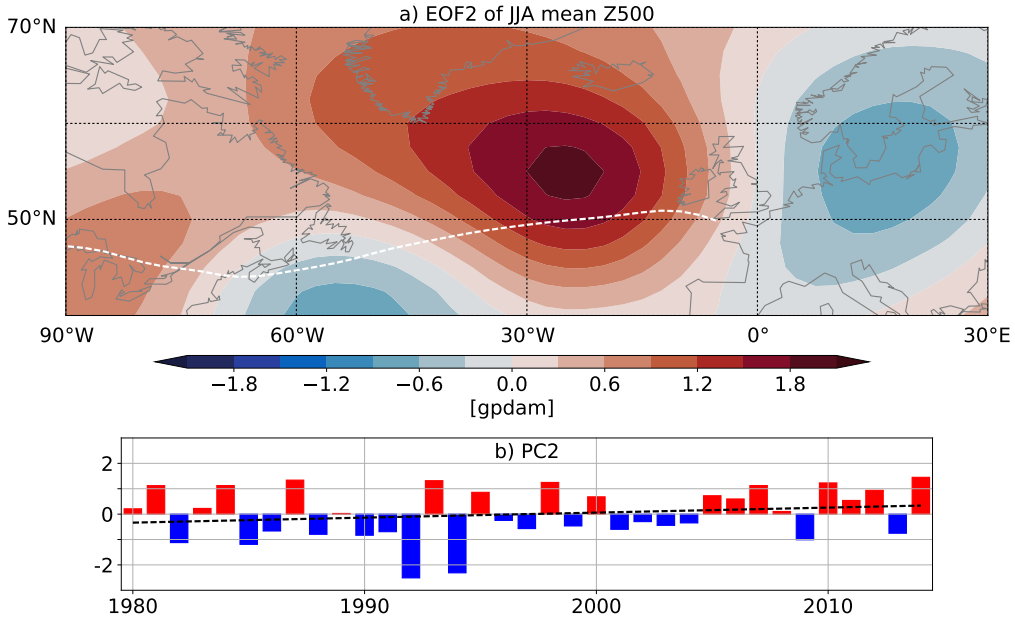

FIGURE 3.5: As in Fig. 3.1 but for the observed SEA (a) pattern (EOF2) and (b) index which explain approximately 18% of the summer z_{500} variance.

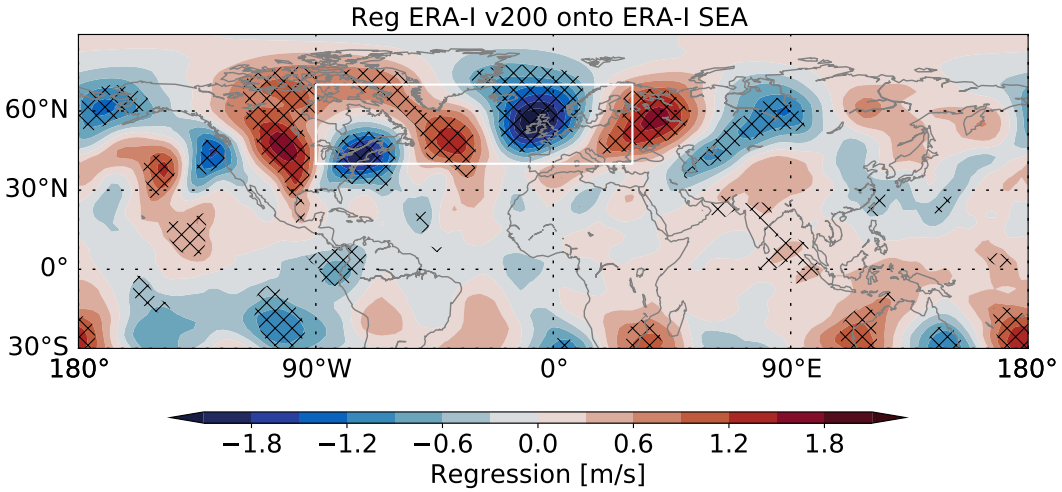

FIGURE 3.6: As in Fig. 3.2 but here for meridional wind at 200 hPa (v_{200}) regressed onto the observed SEA index.

and southward anomalies within the NAE sector and well beyond. It is part of a zonally oriented wave train which corresponds to a meandering jet stream. The positive phase is strongly reminiscent of a blocking pattern. Furthermore, the main centre of the pattern and the weaker node to its east have an equivalent barotropic structure which is evident from the largely similar patterns of the regressions of slp and z_{200} onto the PC2 of z_{500} (Fig. A.4). West of the main centre however, the slp pattern is somewhat different. Due to the similarity of the pattern with the East Atlantic pattern (Barnston and Livezey, 1987), we will name the EOF2 of ERA-Interim JJA mean z_{500} anomalies the summer East Atlantic (SEA) pattern.

The associated PC2 or SEA index (Fig. 3.5b) has a weakly positive linear trend of about 0.20 (decade)$^{-1}$ which is not statistically significantly different from 0.

Relations to other climate variables

Regressing T_{850} onto the SEA index (Fig. 3.7) results in a pattern inside the NAE sector that has a structure almost identical to that of the SEA pattern. At the western and northern edges of the region, significant, positive temperature anomalies extend well over the North American continent, Greenland and the Arctic. East of the NAE sector, the strongest temperature anomaly of up to 0.9 K arises over the Ural mountains, north of the Caspian and Aral Seas. In general, the temperature anomalies reinforce the impression of a wave train associated with the SEA mode as temperature anomalies of alternating sign are organized zonally along the extratropical sector. Additionally, significant temperature anomalies can be found over almost all longitudes in the tropical belt.

In Fig. 3.8, the SST anomaly associated with one standard deviation in observed SEA index is displayed. The pattern is similar in structure to the T_{850} pattern. A strong SST signal of large extent can be observed in the western to central North Atlantic (north of 45°N) with significant temperature anomalies of more than 0.5 K.

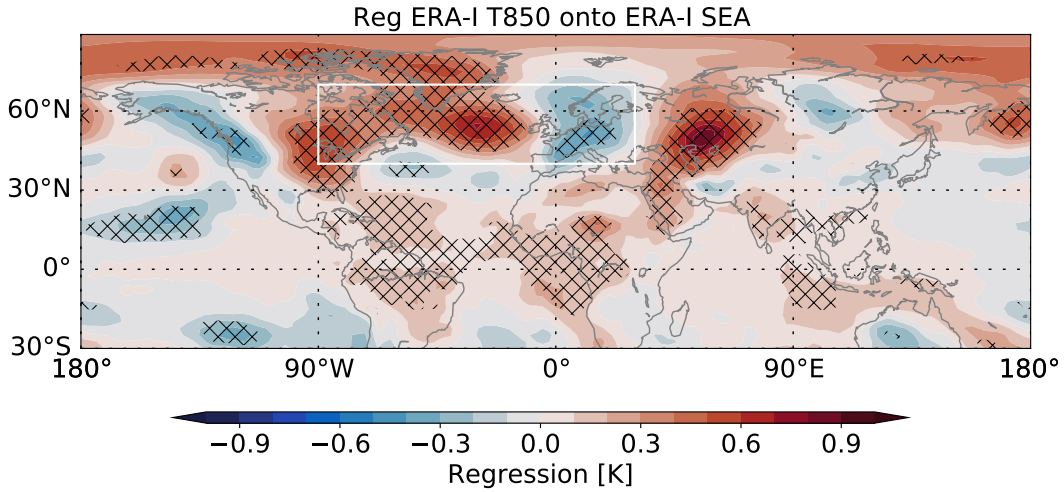

FIGURE 3.7: As in Fig. 3.2 but here T_{850} regressed onto the observed SEA index.

This centre is the northernmost and strongest part of a meridional SST tripole pattern in the western North Atlantic. It involves a negative temperature signal just off the east coast of the United States and another warm band in the tropical Atlantic around the Caribbean and north of South America. Furthermore, small areas in the Beaufort Sea and the Hudson Bay contain the strongest positive temperature anomalies of up to 0.9 K. Another notable structure is observed in the Pacific Ocean. A significant, negative SST anomaly is located in the central to eastern tropical Pacific which is more pronounced north of the equator and extends well into the extratropical North Pacific where it is mostly concentrated in the eastern part. The SST anomalies reach magnitudes comparable to those arising in the tropical Atlantic.

Precipitation anomalies in the NAE sector when regressed onto the SEA index (Fig. 3.9) are weaker and cover a smaller part of the NAE region than when regressed onto the SNAO index (Fig. 3.4). However, in the east of the NAE sector

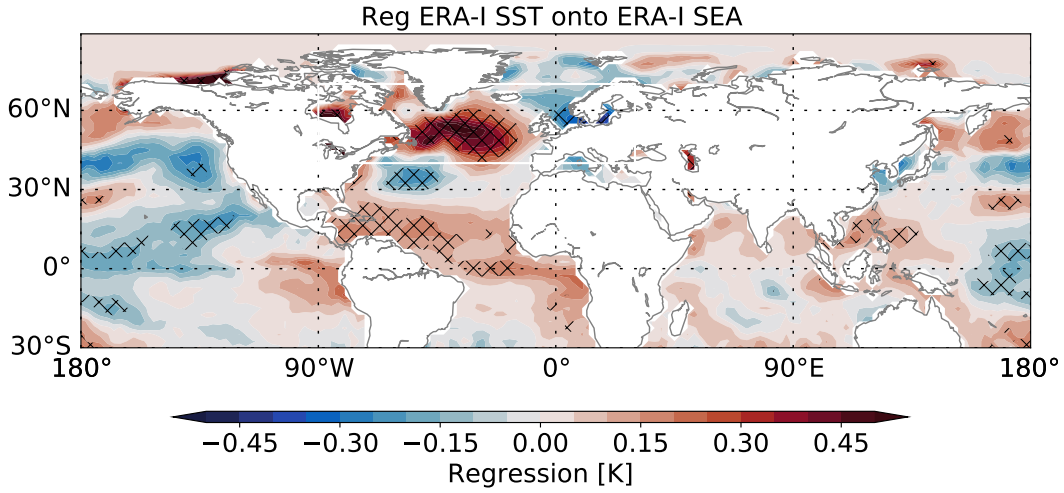

FIGURE 3.8: As in Fig. 3.3 but here SST regressed onto the observed SEA index.

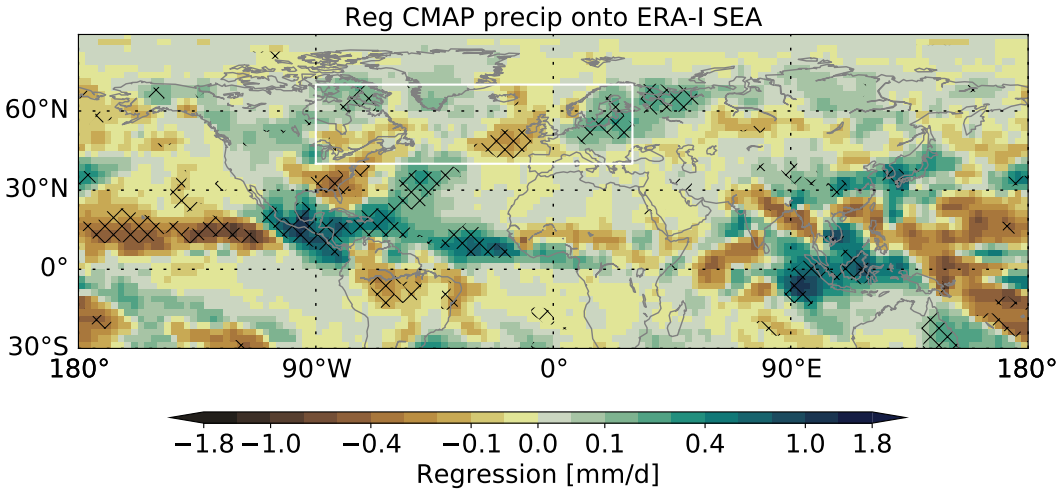

FIGURE 3.9: As in Fig. 3.4 but here CMAP precipitation regressed onto the observed SEA index.

they are also significant. Here, dry anomalies coincide with the major centre of positive z_{500} anomalies of the SEA pattern (North Atlantic and west of the British Isles) whereas east of this, wet anomalies occur where the SEA has negative geopotential height. As before, precipitation anomalies of the largest magnitudes arise throughout the tropics but other than for the SNAO, they are also statistically significant. The most outstanding structure in this regard is a zonal dipole with drier than normal conditions in the central to eastern tropical Pacific north of the Equator and wet conditions over the easternmost tropical Pacific, Central America, southern Mexico and the Caribbean. The wet anomalies even extend into the North Atlantic and the tropical Atlantic up to the west coast of Africa. Centred around the Caribbean wet anomaly, dry anomalies are observed to the south over northern South America and to the north over Florida and the North American east coast. Comparing with Fig. 3.8, it is clear that the area of wet/dry anomalies in the tropical Atlantic/Pacific strongly overlaps with the region of significant, positive/negative SST anomalies related to the SEA index. The co-location of wet and warm SST anomalies is also strong around the Maritime Continent. Note however, that here precipitation anomalies are again among the strongest observed but the regions of significant regressions are rather small and detached from each other.

3.3 Discussion

We have defined the SNAO here as the first EOF of JJA mean geopotential height anomalies at 500 hPa in the NAE sector; it is a robust feature of the boreal summer circulation and has previously been identified as the dominant mode of variability in a number of other studies such as Barnston and Livezey (1987), Greatbatch and Rong (2006), and Folland et al. (2009). The authors of the latter probably provide the most extensive discussion of this mode and its climatic impacts. Even though our definition of the SNAO deviates from that of Folland et al. (2009), the structure is

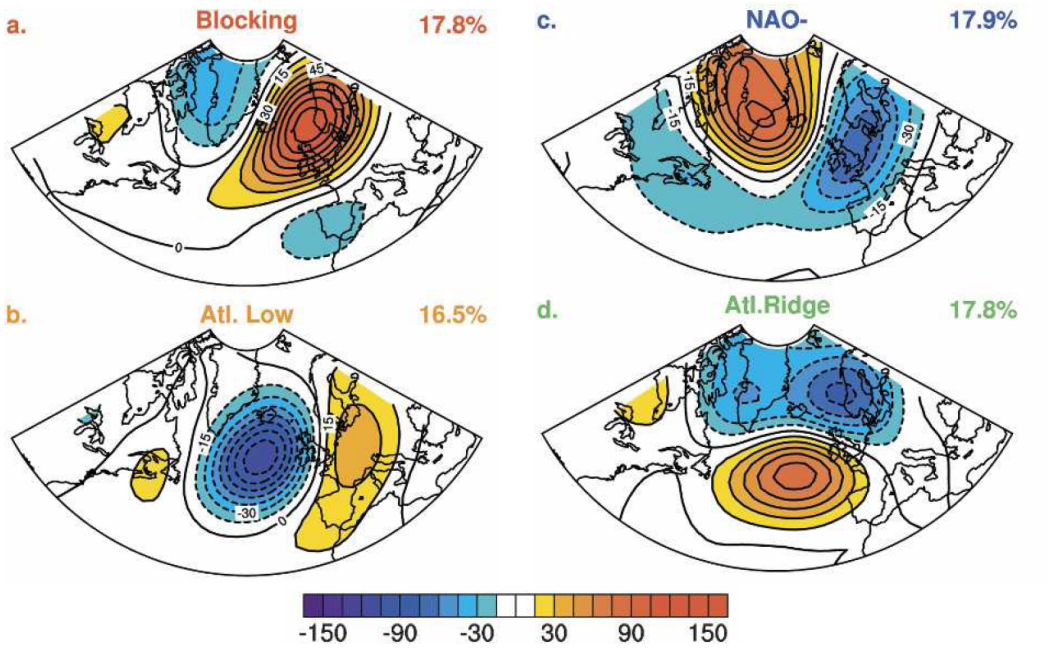

FIGURE 3.10: Figure 1 from Cassou et al. (2005): summer z_{500} weather regimes based on a cluster analysis of daily z_{500} over the region 20°N - 80°N, 90°W - 30°E from 1950-2003 in m (contour interval 15 m). Percentage in the top right corner of each panel shows the relative occurrence of the pattern during that period.

very similar. However, while they find it to explain about 28% of the July-August slp variance, the pattern we define is able to explain as much as 36% of the JJA z_{500} variance. When slp is used to define the SNAO, the resulting pattern even explains 44% of slp variance.

The second mode that we name the SEA however, has attained little - if any - attention to our knowledge. Folland et al. (2009) calculate the second EOF of summer slp over the region 25°N-70°N and 70°W-50°E and find a strongly zonal pattern very unlike our EOF2. In their weather regime analysis of the summer seasons from 1950-2003, Cassou et al. (2005) identify four prevailing regimes of almost equal frequency of occurrence using a non-linear cluster analysis (see Fig. 3.10). Two of these are the positive and the negative phase of the SNAO but with slight spatial asymmetries between them (Fig. 3.10a and c). While their Atlantic Ridge regime (Fig. 3.10d) is very similar to the zonal pattern that arises as the second EOF in Folland et al. (2009), their Atlantic Low regime (Fig. 3.10b) bears close resemblance to the negative phase of our SEA mode. With a linear technique such as PCA we are always limited to finding symmetric patterns, so it might not be quite appropriate in the summer season to identify variability modes other than the SNAO. However, as the SEA mode is a well separated feature in our analysis and its negative phase has been detected by non-linear means of analysis we are confident that to a large part it represents a physical mode of boreal summer variability.

Since from the regression patterns alone it is not possible to determine causality,

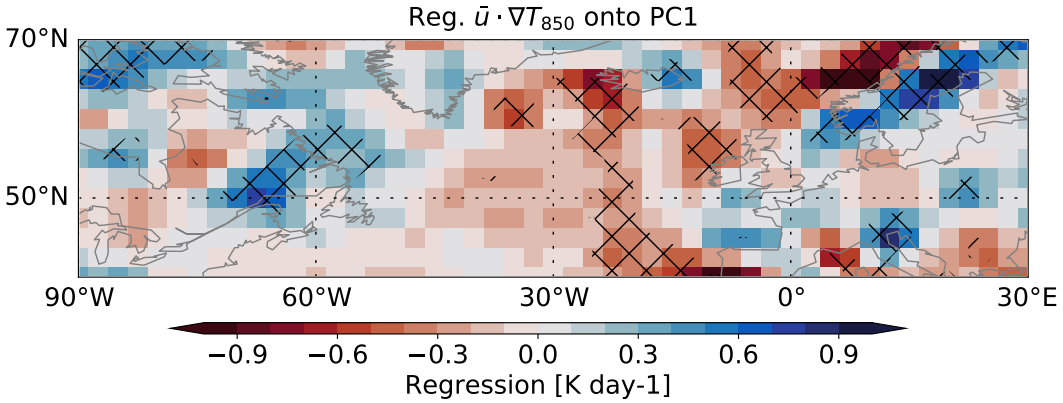

FIGURE 3.11: JJA mean temperature advection $\boldsymbol{u} \cdot \boldsymbol{\nabla} T$ in the NAE region from ERA-Interim regressed onto the observed SNAO index in K day^{-1} per standard deviation in SNAO index. Red colour indicates warm air advection, blue colour cold air advection. Hatching marks where regression coefficients are statistically significant at the 95% level.

physical arguments supporting the influence of the SNAO and SEA on the summer surface climate are brought forward.

Controls on the atmosphere

We consider the atmospheric temperature anomalies inside the NAE sector in Fig. 3.2 to be mostly a response to the anomalous SNAO circulation. Temperature anomalies of one sign coincide with geopotential height anomalies of the same sign, i.e. the structure of the T_{850}/SNAO regression matches almost exactly the SNAO pattern. The reason for this could be the following process: a centre of anomalous anticyclonic/cyclonic flow is associated with large-scale subsidence/ascent which suppresses/enhances cloud formation and thus enhances/suppresses sensible heating at the surface, raising/lowering the surface temperature[2]. This process is supported by Folland et al. (2009) who show that the SNAO is associated with decreased/increased cloud cover in regions of positive/negative slp anomalies. Our precipitation regressions (Fig. 3.4) corroborate this as they mostly show dry/wet conditions in areas of positive/negative height anomalies that are likely to be accompanied by reduced/enhanced cloud cover. However, there is also a notable difference between the SNAO pattern and the T_{850} regression: the temperature anomaly over the British Isles is of larger meridional extent. This points to another control on temperature via the advection of air masses. This is illustrated in Fig. 3.11 which shows the regression of temperature advection onto the SNAO index. South of the anticyclonic node, warm continental air is drawn over Europe by the associated anomalous geostrophic easterly flow. To the north-west of the anomaly, there is a stronger meridional component of the geostrophic flow which also advects potentially warmer air from lower latitudes. This can create a warm anomaly associated

[2]Even though we consider temperature at 850 hPa here the surface heating should be manifest in this variable, too.

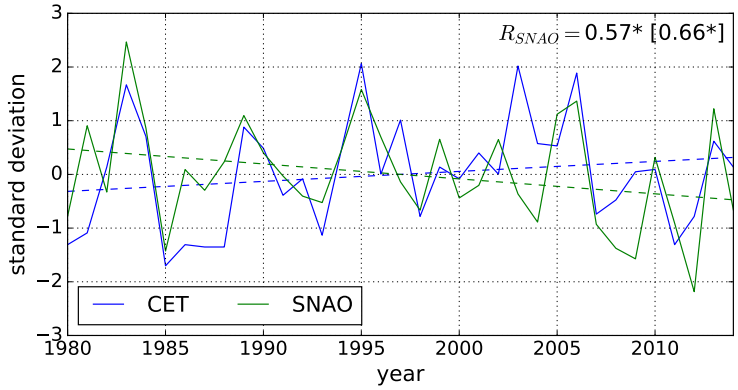

FIGURE 3.12: Time series of (green) the observed SNAO index (as in Fig 3.1b) and (blue) Central England temperature (CET) as normalized JJA mean deviations from the climatological JJA mean. As a result of the normalization, units are standard deviations of the respective time series. Dashed lines show the associated linear trend. Value of R_{SNAO} (in brackets) is the correlation coefficient of the two displayed (detrended) time series. Asterisk denotes significant correlation at the 95%-level.

with the SNAO over Iceland despite lying in a zone where the SNAO pattern itself exhibits anomalies close to zero (Fig. 3.1a). The advection of moisture can also be a relevant factor, e.g. to the south-east of Greenland where wet anomalies occur but coincide with only weak SNAO related z_{500} anomalies. In general, the advective effect, which is dominant for the winter NAO (Hurrell et al., 2003), is also found to be important for the SNAO. However, in summer it is complemented by a radiative effect on the surface heat balance through changes in cloud cover.

To further support the control of the SNAO on European summer surface temperatures, we have considered the SNAO index obtained from ERA-Interim and JJA averaged Central England temperature (CET, Parker et al., 1992) as a true observed surface variable. It can be seen in Fig. 3.12 that both time series are significantly correlated (0.57). Because both controls - the advection of warm air and enhanced surface sensible heating - are at work here, the temperature follows the SNAO index quite closely. Even though the SNAO can account for a large part of the surface temperature variability, it certainly is not the sole process controlling it. This becomes especially obvious if we consider the trend in both time series. While temperature is increasing in the long term, the SNAO tends towards its more negative phase despite the two being positively correlated on interannual time scales. This indicates that on time scales longer than decadal, the SNAO is not the major control on CET. We will return to this issue later.

The regressions of T_{850} and precipitation onto the SEA index (Fig. 3.7 & 3.9) can be - at least in the NAE sector - interpreted in terms of the same mechanisms. In most areas, anomalies of the same sign in z_{500} and T_{850} coincide pointing to the influence of surface sensible heating on temperature as a consequence of large-scale vertical motions. Precipitation on the other hand is inversely related to z_{500} and

T_{850}, especially over the western North Atlantic and northern Europe. Additionally, the advection of cold air by the anomalous southward geostrophic flow could be a factor in driving the significant negative temperature anomalies over France and northern Spain. Cassou et al. (2005) show that extremely high temperatures, especially in France but perhaps in Europe in general, are strongly associated with the positive SNAO phase and the Atlantic Low configuration which resembles the negative phase of our SEA pattern. We note that the extreme summers of 2003 (Black et al., 2004) and 2015 (Duchez et al., 2016) have also been related to large-scale regimes that strongly resemble the negative SEA phase. Thus, there is evidence that also the SEA has important implications for the European summer climate.

Controls on the ocean

The SNAO and SEA associated SST patterns (Fig. 3.3 & 3.8) roughly resemble those of T_{850} (Fig. 3.2 & 3.7) in the NAE sector. It is likely that the sensible heating anomalies associated with the anomalous large scale circulation influence the SST in the same way as mentioned above. Hence, the SST patterns can be a response to the atmospheric forcing. For instance, a difference between the SNAO related patterns (Fig. 3.2 & 3.3) is that the positive SST anomaly around the British Isles is of much smaller meridional extent than its T_{850} counterpart. Due to a lack of the relevant data, we can only speculate about the causes for this. One reason could be related to the different response of the ocean to an altered wind pattern. Ekman transport in the upper ocean as a response to wind stress is directed at a 90° angle to the right of the wind direction (in the northern hemisphere). This could explain the different structure between Fig. 3.2 and 3.3 in the NAE sector. Anomalous geostrophic winds associated with the positive SNAO phase have an eastward component over Iceland. This will lead to anomalous southward Ekman transport of colder polar water, thus creating a broader cold anomaly to the south-west of Iceland and a narrower warm anomaly around the British Isles. Another possible reason is an increased/decreased turbulent heat flux from the ocean to the atmosphere through higher/lower wind speeds. In general of course, both mechanisms could be factors in generating the SST anomalies associated with the SEA, too.

At this point, it is important to note that two-way interactions between the atmosphere and the ocean can also be reflected in the observed regressions. Czaja and Frankignoul (1999) show that there can be an influence of summer SST anomalies onto the NAO in the succeeding winter. Using a lead/lag maximum covariance analysis (MCA), Gastineau and Frankignoul (2015) find that squared covariance between boreal summer SST and z_{500} is significant when the atmosphere leads by up to 3 months (and possibly beyond) but also when the ocean leads by up to 4 months. In fact, we find strong resemblance between the z_{500} part of the dominant MCA mode when the atmosphere leads the ocean by one month (Gastineau and Frankignoul, 2015) and the observed SNAO. This supports our reasoning that the observed SST

regression pattern (Fig. 3.3) in the NAE sector shows the response of the upper ocean to the atmospheric forcing by the SNAO. However, the authors also show a significant atmospheric response to SST anomalies after 3 months that is also reminiscent of the SNAO. We conclude from this that by considering simultaneous regressions of seasonal means, our patterns may well include a signature of these two-way interactions even though the atmospheric response should be smaller due to the approximate oceanic lead time of 3 months which is the upper limit of what we can capture with seasonal averages.

Keeping this in mind, we point out another strikingly similar feature of the study of Gastineau and Frankignoul (2015) and this thesis. The atmospheric part of their dominant MCA mode when the ocean leads by 3 months has a pronounced z_{500} anomaly with its centre at approximately 53°N and 20°W which is much like our observed SEA pattern. Furthermore, the oceanic part of their pattern is similar to the regression of SST onto the SEA index (Fig. 3.8). Using reanalysis data, Duchez et al. (2016) show that the 2015 European heat wave was accompanied by an atmospheric circulation regime much like the negative SEA phase. They argue that it was a result of an exceptionally cold SST anomaly in the North Atlantic. This SST anomaly also projects well onto the SST/SEA regression (Fig. 3.8). This is an indication that this regression pattern can also contain an imprint of local air-sea feedbacks inside the NAE region.

4 Remote impacts on the NAE summer climate

In the regression maps of the previous sections, some areas outside of the NAE region where certain climate variables strongly covary with the dominant modes of variability could be identified. Using a regression, it is not possible to separate a response from a forcing. To overcome this issue, the relaxation experiments (section 2.1.3) are analysed using the techniques described in section 2.2.6. This will allow us to identify forcings from the relaxation regions provided the models are able to simulate these correctly. The plausibility of the identified forcings is then tested by considering the possible mechanisms by which they influence the NAE summer climate.

4.1 Relaxation experiments

A measure of the skill of the relaxation experiments in predicting the full interannual summer variability is the z_{500} anomaly correlation coefficient (ACC) which is shown in Fig. 4.1. The ACC is the correlation of the detrended reanalysis with the detrended ensemble mean time series at each grid point. For CLIM-ARC, CLIM-TROPICS and OBS-TROPICS it is obvious where the models are relaxed towards ERA-Interim; in these areas the ACC is effectively 1 (dark red).

As mentioned in section 2.1.3, the relaxation parameter is non-zero as far as approximately 10° outside of the boundaries given in Table 2.1. As a consequence, the atmosphere north of 65°N must be considered relaxed in CLIM-ARC. The NAE sector's northern limit is 70°N, so the two regions have an overlap of 5°. This needs to be kept in mind when evaluating the skill of this experiment. It is evident that there is also significant skill in CLIM-ARC south of 65°N. Over western Siberia, Greenland and central to eastern Canada, strong correlations extend furthest south. Away from these regions, significant correlations occur but are weak, of small spatial extent, and of positive and negative sign an approximately equal number of times; these are likely to be false positive results.

Interestingly, there are more areas outside of the Arctic in CLIM-NO than in CLIM-ARC in which the skill of the model is significant despite the lack of an anomalous forcing in CLIM-NO. These are the eastern subtropical Atlantic, the southern Mediterranean and the north of Libya and Egypt, the western Pacific east of Japan

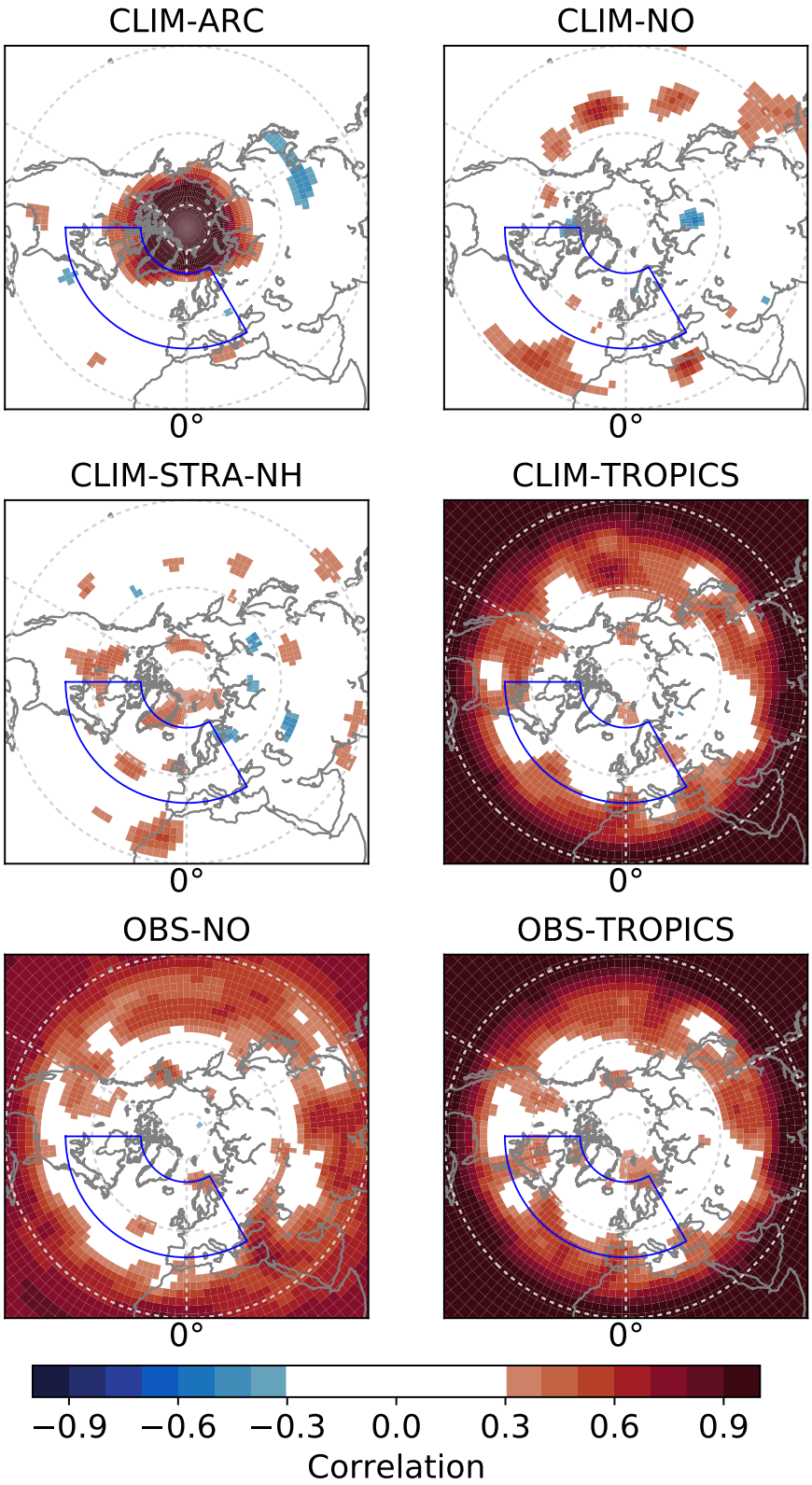

FIGURE 4.1: ACC for detrended JJA mean z_{500} between ERA-Interim and the ensemble mean forecast of the experiment as indicated in the title. Only correlations that are significantly different from 0 on the 95% level based on a t-test without account of serial correlation are coloured. Latitudes are marked by dashed grey circles in intervals of 30°. Outer circle marks 20°N. Blue line indicates the NAE sector.

and parts of the central North Pacific. The structure in the Pacific region is reminiscent of a wave train. The skill in CLIM-NO suggests that there is some predictability arising from the memory of the initial conditions. Since these are the same for all experiments, it is curious that neither in CLIM-ARC nor in the stratospheric relaxation experiment the same areas show up.

Significant skill in CLIM-STRA-NH is found in a region extending from Greenland to Svalbard and over the Barents Sea, one in central Canada, and one over the north-western African coast. However, the correlations appear to be rather on the order of false positive results that we would expect using a 95% significance threshold.

CLIM-TROPICS exhibits many areas in the extratropics where the skill is significant. The effect of tropical relaxation is most pronounced over North America, the central to western North Pacific and east Asia. The pattern is very similar when SST/SI is prescribed, i.e. in OBS-TROPICS. The most marked difference in OBS-TROPICS is over North America, where CLIM-TROPICS performs better while over the western North Atlantic, OBS-TROPICS does.

Although the tropical atmosphere is not relaxed in OBS-NO, this set-up shows high ACC in the tropical sector. This is due to the fact that the tropical circulation is strongly governed by the underlying SST (Charney and Shukla, 1981). As a result of reproducing the tropical atmospheric state well, this experiment also exhibits significant skill in the extratropics much like the experiments with tropical relaxation. However, the extratropical skill is generally weaker than, and does not extend as far north as, in CLIM-TROPICS and OBS-TROPICS except over the eastern Mediterranean and to its north-east.

Although there is clearly some extratropical skill in various regions in most experiments, simulation of the summer variability inside the NAE sector is generally poor. The skill of the Arctic and tropical relaxation experiments is perhaps most promising, even though in the former it needs to be treated with care.

Up to now, we have considered the skill of the ensemble means of the relaxation experiments in reproducing the full observed interannual boreal summer variability. However, if there is a forcing from a relaxation region of one of the modes of variability described in the previous chapter, we will gain some extra insight by considering how the models forecast each of these individually.

Simulation of the SNAO

By comparing the blue and orange lines in Fig. 4.2, we can see how the ensemble mean of each experiment reproduces the observed SNAO. It is obvious that the ensemble mean SNAO in all experiments has smaller variance than the observed SNAO. Since the observations represent a single realization, the observed SNAO signal must contain internal variability. By ensemble averaging, we are reducing the natural variability, so the ensemble mean simulated SNAO is expected to have

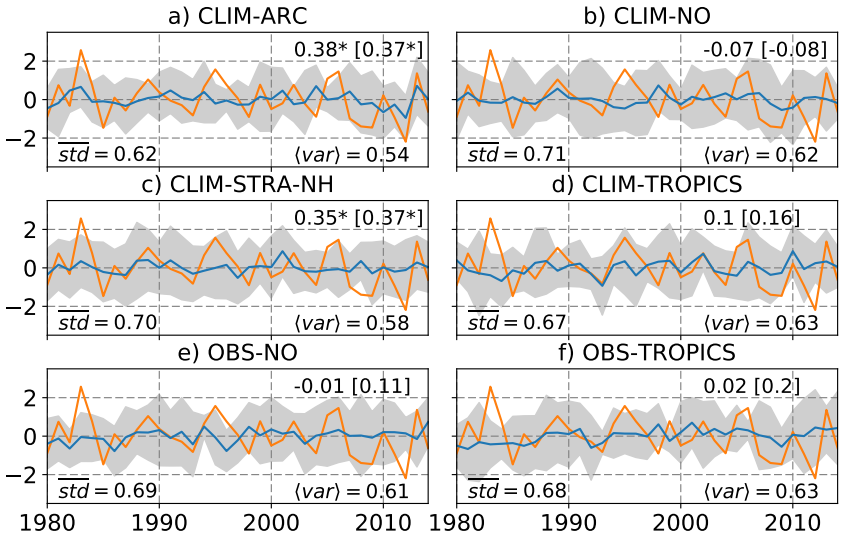

FIGURE 4.2: Time series of observed and projected SNAO for relaxation experiments as indicated in the title. Orange line: observed SNAO. Blue line: ensemble mean projected SNAO. Number (in brackets) in the top right of each panel is the correlation coefficient between these two (detrended) time series. Grey area indicates two standard deviations around the ensemble mean projected SNAO, given by the projected SNAOs of the 9 single members. The standard deviation of the ensemble members averaged over time ($\overline{std}$) is shown in the bottom left of each panel. Variance of the full ensemble ($\langle var \rangle$) is displayed in the bottom right.

smaller variance. While it is very small in CLIM-NO and CLIM-STRA-NH (about 7% of the observed variance), it is larger in the other 4 experiments (11-14%).

The variance of the simulated SNAO based on all ensemble members is given as $\langle var \rangle$ in the panels of Fig. 4.2. Since the simulated SNAO is normalized by the standard deviation of the observed SNAO, this value expresses the fraction of variance of the observed SNAO that the ensemble reproduces. Curiously, even the full ensembles of the experiments with the highest variance only capture 63% of the observed SNAO variance.

The grey envelope around the blue line in Fig. 4.2 shows the spread of the ensemble around the ensemble mean simulated SNAO in which approximately 95% of the single ensemble projected SNAO values fall[1]. This serves to indicate how likely an observed SNAO event is under the forcing present in the experiment. It is notable that all but three events (1983, 1995 and 2012) are possible outcomes of the experiment without anomalous forcing (CLIM-NO), indicating that most years are consistent with what is mostly internal variability in this experiment. The two strongest SNAO (1983, 2012) events exceed 2 standard deviations and fall outside of the grey shading in all experiments, suggesting they are highly unlikely under any of the considered forcings. The strongly positive SNAO of 1995 is a possible realisation of CLIM-STRA-NH and CLIM-TROPICS but is also smaller in magnitude than the other two events.

[1]Note that this is based on only 9 members and thus a only a rough estimate

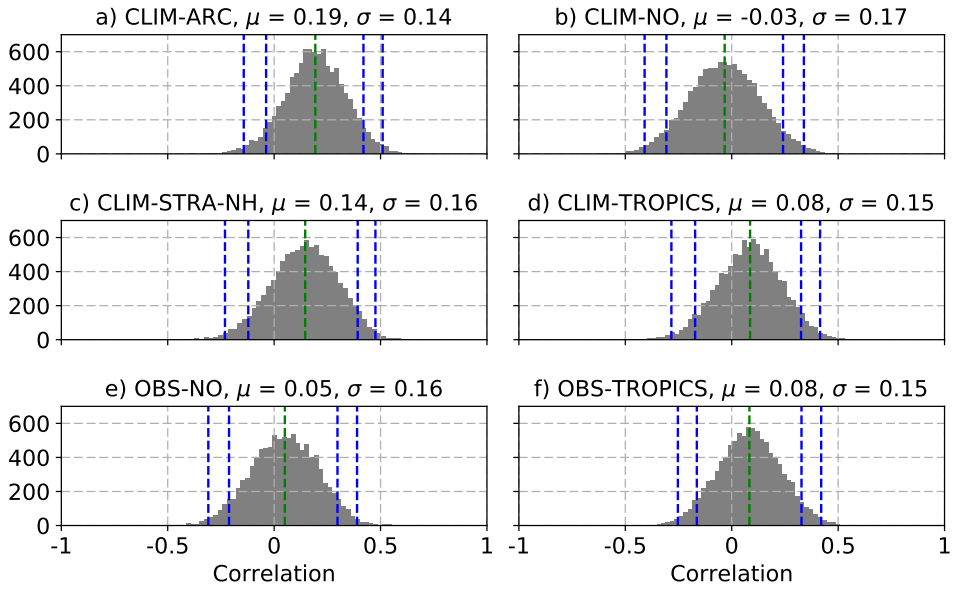

FIGURE 4.3: Histograms (50 bins) of 10,000 bootstrapped interannual correlations between detrended time series of observed and projected SNAO (as explained in section 2.2.6). Blue dashed lines indicate the 1st, 5th, 95th and 99th percentile of the distribution, green dashed line the median. μ and σ in the title of each panel are the empirical mean and standard deviation of the correlation distribution respectively.

The mean width of the grey envelope is measured by $\overline{std}$. This value is defined as the spread of the ensemble around its mean at each time step averaged over the 35 year simulation period. This measure indicates how strongly the internal SNAO variability in an experiment is constrained by the forcing. If there were a significant forcing from one of the relaxation regions, we would expect to see a lower value of $\overline{std}$ in that particular experiment compared to the other runs. For the SNAO, the values of $\overline{std}$ are similar in all experiments. Only CLIM-ARC has slightly lower $\overline{std}$ and can be said to more strongly constrain the internal SNAO variability than the other experiments.

The skill of an experiment in simulating the observed SNAO is measured by the correlation coefficient between the observed and ensemble mean simulated SNAO (indicated in top right corner of each panel of Fig. 4.2). Out of the 6 experiments, only CLIM-STRA-NH and CLIM-ARC exhibit significant skill while the rest mostly fails to reproduce any of the SNAO variability at all (correlations ≤ 0.1). However, the skill of CLIM-TROPICS, OBS-NO and OBS-TROPICS increases when both the observed and the simulated SNAO are detrended (correlation value in brackets), i.e. they do better at simulating the interannual variability. In these experiments the long-term trend is positive rather than negative as in the observations. CLIM-ARC and CLIM-STRA-NH on the other hand do not only reproduce the interannual but also the long-term variability reasonably well.

In Fig. 4.3, we show the distribution of correlations between the detrended observed SNAO and 10,000 bootstrapped detrended SNAO projections (see section

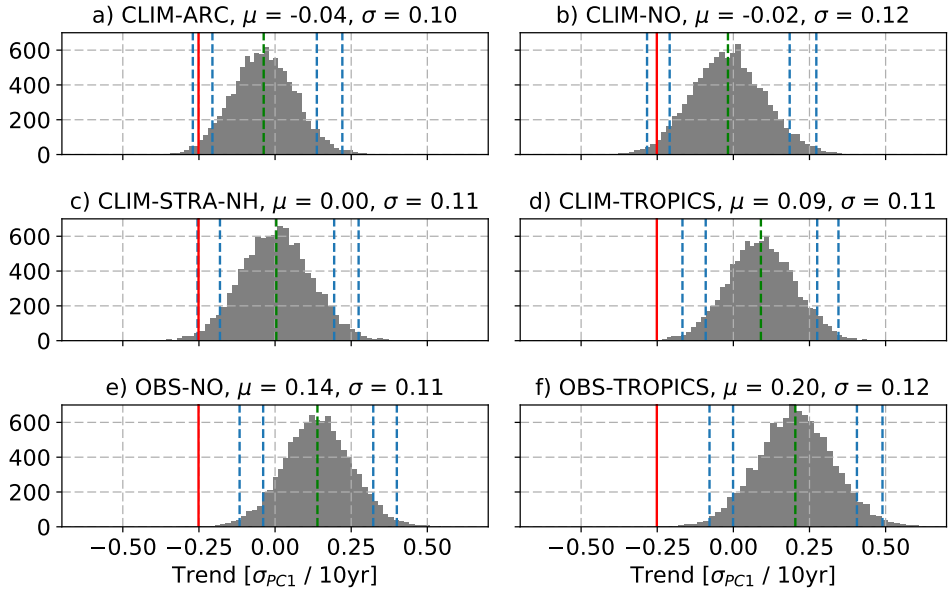

FIGURE 4.4: Histogram (50 bins) of 10,000 bootstrapped SNAO trends (as explained in section 2.2.6) in units of one standard deviation of the bootstrapped SNAO per 10 years. Blue dashed lines indicate the 1st, 5th, 95th and 99th percentile of the distribution, green dashed line the median. The red solid line shows the linear trend of the observed SNAO in units of one standard deviation of the observed SNAO per 10 years. μ and σ in the title of each panel are the empirical mean and standard deviation of the trend distribution respectively.

2.2.6 for a description of this procedure). If the distribution is strongly shifted away from 0 towards positive values, we will take this as an indicator of a forcing for the SNAO from the relaxation region. Our confidence in this will be higher, the larger the mean μ of the distribution is compared to its standard deviation σ. Unsurprisingly, correlations in CLIM-NO are centred approximately around 0. This is to be expected considering that the single summers in this experiment only vary by their different initial conditions. The distributions of CLIM-TROPICS, OBS-NO and OBS-TROPICS are only slightly shifted towards positive values. Since $\mu < \sigma$ in these, a forcing is not clearly distinguishable. Even though the distribution for the stratospheric relaxation experiment is more strongly shifted than in the aforementioned cases, again $\mu < \sigma$ and correlations of 0 are not unlikely under this forcing. When the analysis is repeated using monthly instead of seasonal anomalies, CLIM-STRA-NH exhibits a shift that is rather weak and comparable in magnitude to that of all other experiments except CLIM-ARC. Only under Arctic relaxation does the histogram have $\mu > \sigma$ (also on a monthly basis). It remains to be noted that the width of all distributions (as measured by σ) is approximately equal in all experiments and hence, none of the forcings constrains the internal SNAO variability.

When we consider the simulation of the SNAO time series in Fig. 4.2, we can see

that even though the negative trend in the observed SNAO is not statistically significant, the models with tropical relaxation and prescribed SST/SI performed significantly better when considering the interannual variability alone while detrending did not make a difference for CLIM-ARC or CLIM-STRA-NH. We now want to consider how likely the observed trend is under the forcing of each experiment. In Fig. 4.4, we show the histogram of 10,000 bootstrapped linear trends of the SNAO for the 6 relaxation experiments. The trend distribution of CLIM-NO is again centred around 0 consistent with no anomalous forcing in this set-up. The observed trend falls between the 1st and 5th percentile of its distribution and hence is quite unlikely to occur as part of the model's internal variability. The trend is also quite unlikely under Arctic and stratospheric forcing. In both these experiments, bootstrapped trends are generally centred around 0. This is different in the tropical relaxation and prescribed SST/SI experiments. The distributions of these are rather strongly shifted towards positive trends, for prescribed SST/SI even $\mu > \sigma$. Curiously, tropical relaxation and prescribed SST/SI seem to force positive trends in the projected SNAO, rendering any negative trend highly unlikely in these configurations. This raises the question of how the observed trend is forced and why the tropical relaxation experiments and OBS-NO produce a trend of opposite sign.

Simulation of the SEA index

The simulation of the observed SEA index is displayed in Fig. 4.5. As for the SNAO, the ensemble mean of all experiments has a smaller variance than the observed index but for the SEA large differences between the experiments are evident. The ensemble mean SEA indices of CLIM-NO and CLIM-STRA-NH both have smallest variance (5% and 6% resp.). Variance is larger in the ensemble means of CLIM-TROPICS (11%), even greater in OBS-NO and OBS-TROPICS (17% and 18% resp.) and highest

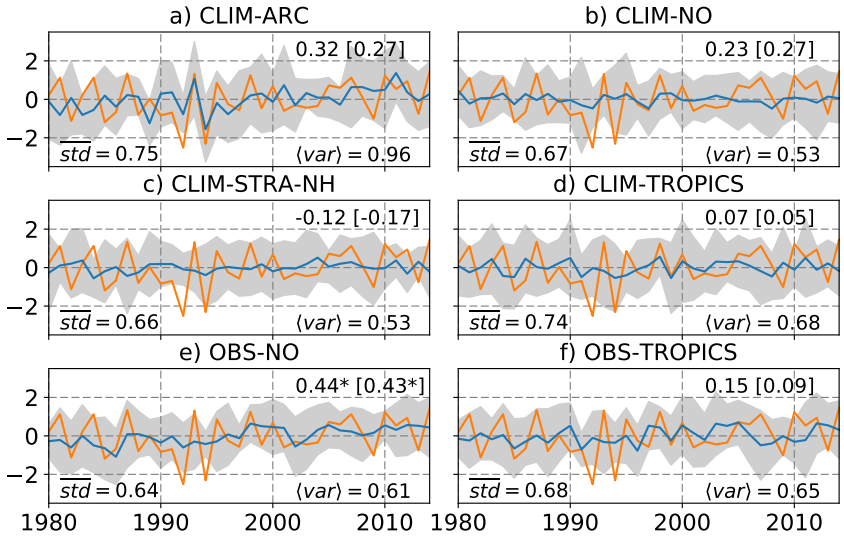

FIGURE 4.5: As in Fig. 4.2 but for the SEA index.

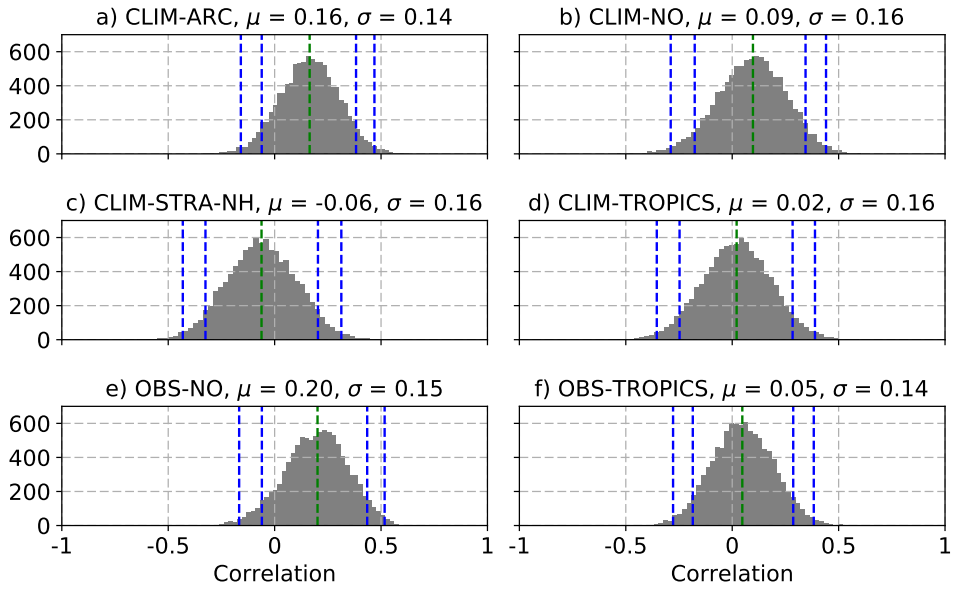

FIGURE 4.6: As in Fig. 4.3 but for the SEA index.

in CLIM-ARC (36%). Moreover, the full ensemble variance of CLIM-ARC is 96% of the observed SEA variance while all other experiments produce much lower SEA variance (between 53 and 68% of the observed SEA variance). This indicates that relaxation of the Arctic atmosphere imposes a rather strong constraint on the SEA mode. As pointed out before, an influence from the overlap of the Arctic relaxation region and the NAE sector cannot be ruled out as an influence.

Next, the spread of the ensembles is considered (grey envelope in Fig. 4.5). Only the two strongly negative observed SEA events of 1992 and 1994 are found to lie outside of the spread of the CLIM-NO ensemble. They both exceed two standard deviations of the observed index. The stronger of the two (1992) is not captured by the ensemble spread of any experiment. The 1994 SEA event on the other hand is a possible outcome of the CLIM-ARC and CLIM-TROPICS ensembles. That they simulate this event is partly due to the large spread of these ensembles. CLIM-ARC and CLIM-TROPICS have the highest value of $\overline{std}$ out of all experiments.

In terms of skill of the ensemble mean, only OBS-NO stands out with a significant correlation between observed and ensemble mean simulated SEA. Curiously, it performs much better than OBS-TROPICS that uses the same lower boundary forcing but contains extra information about the true tropical atmospheric state. The same can be said about the skill in CLIM-NO and CLIM-TROPICS that are equally related. Even though CLIM-ARC reproduces the largest part of the observed SEA variance it does not exhibit significant skill in simulating its year-to-year variability.

Re-sampling of the projected SEA confirms the results of the analysis of the projected SEA time series: the standard deviation σ of the histograms does not differ significantly between the experiments. Only in OBS-NO the distribution is significantly shifted away from 0 ($\mu > \sigma$) towards positive values (see Fig. 4.6). It is

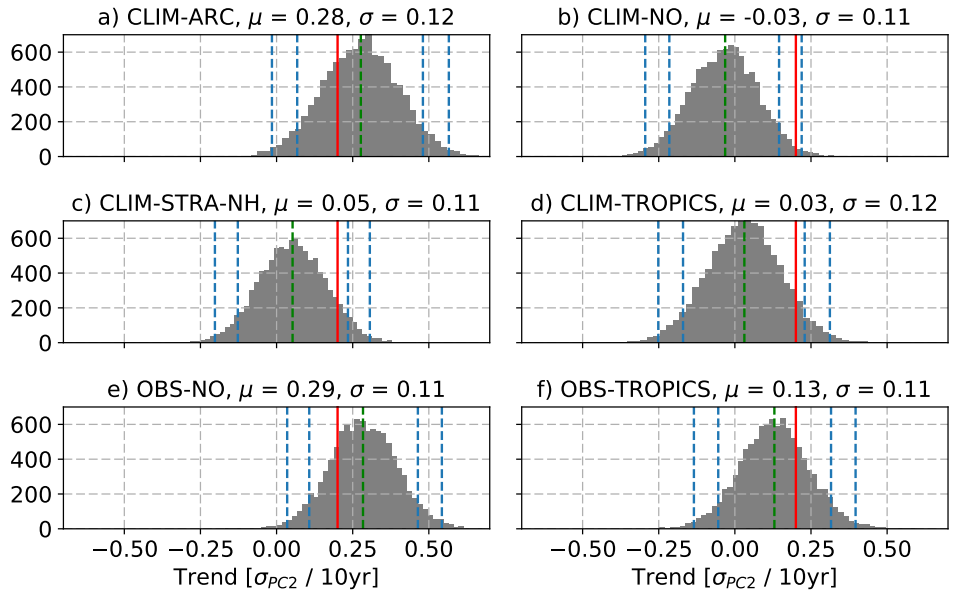

FIGURE 4.7: As in Fig. 4.4 but for trends in the SEA index.

apparent that for simulating SEA related variability, specifying SST/SI is of importance.

The experiments without relaxation (CLIM-NO and OBS-NO) perform better than their counterparts with tropical relaxation (CLIM-TROPICS and OBS-TROPICS), independent of whether SST/SI is prescribed or maintained. This is surprising considering that these two experiments use the same boundary conditions but the tropical relaxation experiments actually contain a more accurate estimate of the true state of the tropical atmosphere. The tropical relaxation clearly degrades the model's skill in simulating the SEA.

As for the SNAO, we also address the trend of the SEA index. When we consider Fig. 4.7, we can see that the observed trend lies between the 95th and 99th percentile of the simulated SEA trends and is thus rather unlikely in CLIM-NO. For all other experiments, the observed trend is located between the 5th and the 95th percentiles of the histograms and is a likely outcome under any of the forcings. It should also be noted that under prescribed SST/SI and Arctic relaxation, a positive trend has a high probability of occurring, perhaps pointing to an influence of sea-ice on the long-term variability of the SEA.

4.2 A tropical forcing of the SEA?

4.2.1 Tropical precipitation

In chapter 3, we saw that there is a strong relationship of the observed SEA with precipitation and SST in the Caribbean and the central tropical Pacific. Additionally, in the previous section, it became evident that prescribing SST/SI has an effect on

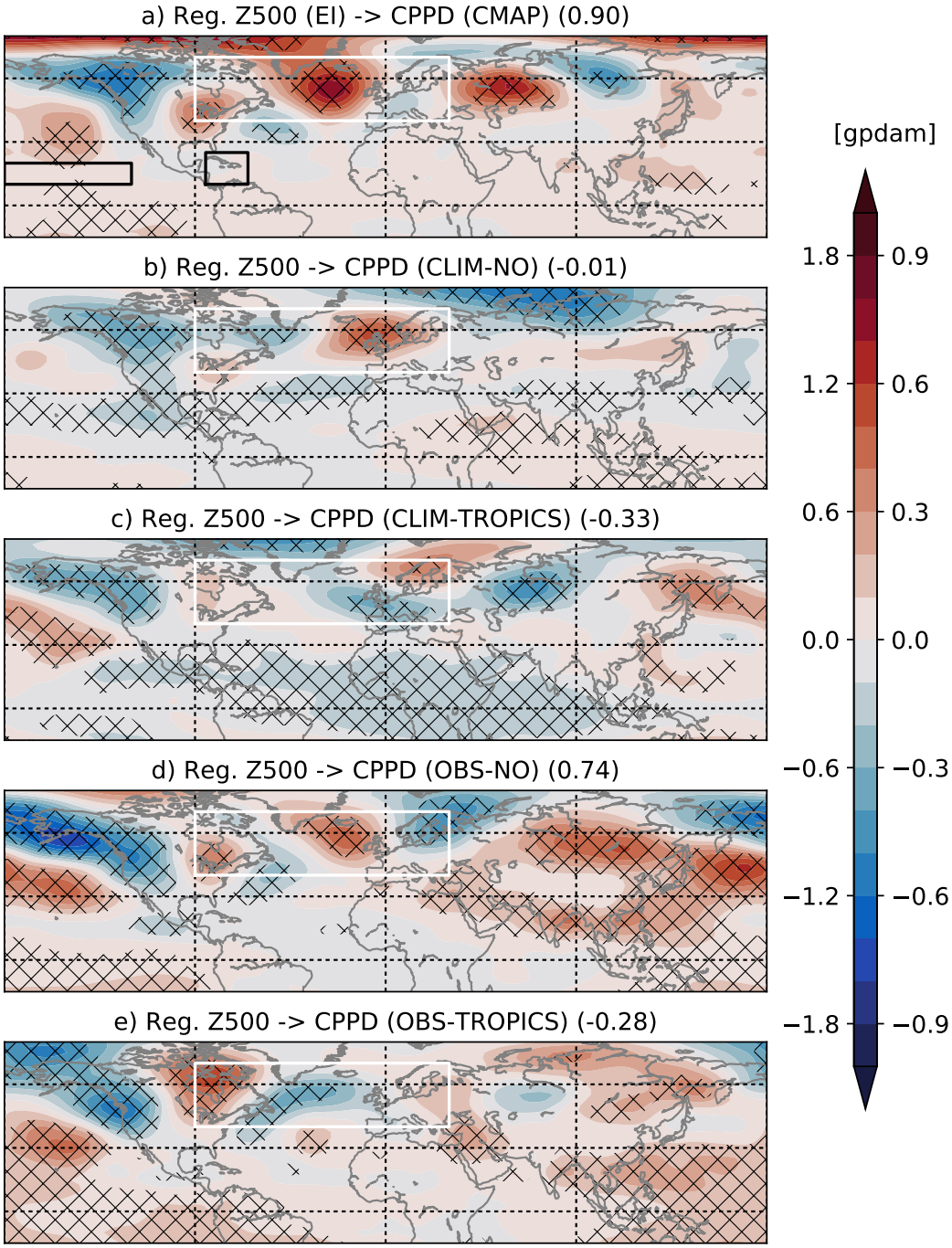

FIGURE 4.8: (a) Regression of JJA mean z_{500} from ERA-Interim onto CPPD from CMAP. (b-e) Regression of z_{500} onto CPPD, both from the full ensemble of the experiment indicated in the title. The z_{500} field and CPPD are detrended prior to regressing. Units are gpdam per one standard deviation in CPPD index. Labels on the left of the colour bar refer to a); labels on the right apply to b) - e). Hatching shows where regression coefficients are significantly different from 0. By using the full ensemble, the time series are 9 times as long as for ERA-Interim, hence the lower significance threshold in b) - e) compared to a). White box indicates the NAE sector, black boxes the region over which precipitation was averaged for the CPPD (limits given in text). PCC between the regression pattern of the respective dataset in the NAE region and the observed SEA pattern is shown in parentheses in the title of each panel.

predicting the observed SEA although the model results were not entirely conclusive. Motivated by the robust statistical link between the SEA and Caribbean and Pacific precipitation and SST, we calculate the regression of JJA mean z_{500} anomalies onto an index of convective activity in both the central tropical Pacific and the Caribbean. This index is defined as the normalized difference between precipitation averaged over a region in the Caribbean (85°E - 65°E, 10°N - 25°N) minus precipitation averaged over a region in the central tropical Pacific (180°E - 120°E, 10°N - 20°N)[2] and is hereafter referred to as the Caribbean-Pacific precipitation dipole (CPPD). When computed from CMAP precipitation, this index is highly correlated with the observed SEA index (0.54, statistically significant at the 95% level). The results presented in the following are not sensitive to the choice of the box boundaries. They hold similarly if only one of the boxes is used and also if SST is used instead of precipitation to define the index.

The regression of ERA-Interim z_{500} anomalies onto the CPPD index computed from CMAP is shown in Fig. 4.8a. It becomes evident that in several regions in the extratropics, z_{500} significantly co-varies with the dipole. The regression pattern resembles a wave train with zonal wave number 5 emanating from the central to eastern North Pacific. This wave train stretches north-eastward and appears to be refracted southward over the North American continent. Entering the NAE region, it then extends further south-eastward and is reflected in the sub-tropical Atlantic towards the eastern North Atlantic. It then extends beyond the eastern limit of the NAE region into Siberia. Inside the NAE sector, the wave pattern projects strongly onto the SEA pattern (PCC of 0.90). The z_{500} signal associated with one standard deviation in CPPD is even of similar magnitude as the z_{500} anomalies for one standard deviation in SEA. This is a strong indication for a tropical diabatic forcing of the SEA pattern which appears to be a part of a hemisphere-wide wave train.

To address the question why the tropical relaxation experiments fail at predicting the SEA despite the apparent tropical forcing, we redo the regression analysis from above but using anomalies of z_{500} and precipitation from the full model ensembles (Fig. 4.8b-e). For this purpose, the output fields from the 9 ensemble members of each experiment are concatenated along the time axis. By doing so, the number of time steps is increased from 35 to 315.

Clearly, in CLIM-NO (Fig. 4.8b), regression coefficients are much smaller than in the reanalysis. In the origin region of the wave train, CLIM-NO reproduces the observed signal fairly well but only the negative height anomaly over western North America is statistically significant. The pattern that arises in the NAE sector is only weakly related to the observed SEA pattern. The failure of this experiment in simulating the wave train is mostly owed to the fact that it does not predict precipitation in the CPPD regions well (not shown) due to the use of climatological SST in this set-up. OBS-NO (Fig. 4.8d) exhibits a wave train that originates in the North Pacific

[2]CMAP precipitation averages over these boxes are correlated at -0.43 which is statistically significant at the 95% level.

much like the observed one. The wave train in OBS-NO also bends eastward and extends zonally into the NAE sector. East of the NAE sector, however, the signature looks somewhat different from the z_{500} relation in ERA-Interim. There, significant anomalies that extend around the globe back to the origin of the wave train are found. The most important result of the regression pattern in OBS-NO is that the pattern inside the NAE sector also projects strongly onto the observed SEA pattern (PCC of 0.74) which explains why this experiment has significant prediction skill for the SEA.

In Fig. 4.8c and e, it becomes obvious that the origin of the wave train over the North Pacific is also reproduced by the tropical relaxation experiments. However, over the North Atlantic, the signature is very different. Especially in OBS-TROPICS, the wave train enters the NAE region extending south-eastward. Instead of being reflected back towards the eastern North Atlantic like in ERA-Interim and OBS-NO, the wave then extends into the tropics where it vanishes. As a result of the dissipation of the wave, the tropical relaxation experiments cannot reproduce the main anomaly of the SEA pattern.

To further analyse the reason for this we examined the skill in simulating the precipitation in the CPPD boxes by calculating the correlation with CMAP. For OBS-NO and OBS-TROPICS, the skill is similarly high (between 0.76 and 0.79) and thus the simulation of tropical Pacific and Caribbean precipitation cannot be the main problem in predicting the SEA mode. Under the assumption that the CPPD exerts a major control on the SEA pattern, this indicates that the reason for the failure of CLIM-TROPICS and OBS-TROPICS in predicting the SEA lies in the modification of the CPPD related wave train. This modification must be associated with the relaxation itself since this is the only difference between OBS-NO and OBS-TROPICS.

4.2.2 Rossby wave source activity

As described in chapter 1, tropical convection is a major source for planetary Rossby waves. In the presence of westerly winds and sufficient meridional potential vorticity gradients, these can propagate well into the extratropics and as a result impose a forcing on variability in areas far away from their source region. We were able to identify a Rossby wave-like pattern related to precipitation in the tropical Pacific and the Caribbean. We now seek to confirm that this mechanism is at work in inducing the SEA pattern. This is done by examining if there is RWS activity in the vicinity of the CPPD area related to variations in both the CPPD and the SEA index. The regression of the seasonal mean RWS at 200 hPa onto the CPPD is shown in Fig. 4.9a, where ERA-Interim was used to compute the RWS and CMAP for the CPPD. There is significant, positive RWS activity over the tropical central to eastern Pacific inside the zone of JJA climatological mean easterlies. Another significant, positive RWS anomaly is found in the Arctic, north of the Beaufort Sea. The most pronounced

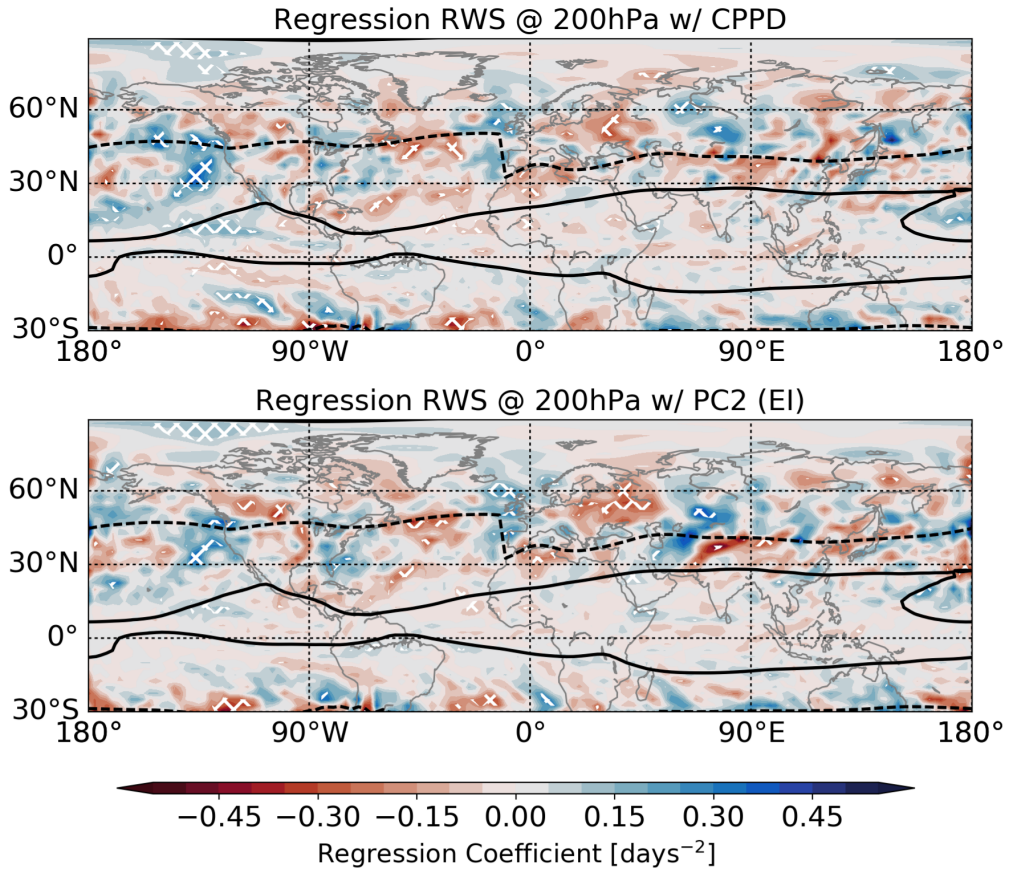

FIGURE 4.9: Map of RWS at 200 hPa (computed from ERA-Interim) regressed onto the a) CPPD (CMAP) and b) SEA index (ERA-Interim). Shading shows the regression coefficient in days^{-2} per one standard deviation in the respective index. Blue indicates sources of positive (cyclonic) vorticity while red indicates sources of negative (anticyclonic) vorticity. The solid black lines mark the zero-line of climatological mean JJA zonal wind u_{200} with westerly zonal winds north of the northern and south of the southern line and easterlies between them. The dashed black line shows the location of the meridional maximum of climatological mean JJA u_{200}.

signal occurs over the eastern North Pacific, and stretches over the North American west coast and the coast of Alaska. This RWS lies in the vicinity of the upper tropospheric jet stream (indicated by the black dashed line in Fig. 4.9) and is consistent with the CPPD related wave train in Fig. 4.8a. It indicates that positive, i.e. cyclonic vorticity (blue colour in Fig. 4.9a) is generated west of the North American west coast. This is in agreement with the trough (blue colour in Fig. 4.8a) that lies downstream of this source. It can be seen that sources of alternating sign are located downstream of the main source well into the NAE region. It is notable that in general the troughs/ridges (blue/red in Fig. 4.8) lie downstream of cyclonic/anticyclonic RWSs (blue/red in Fig. 4.9a). These sources, though only partly statistically significant, are entirely consistent with the anomalies of the wave train. Even though they are not statistically significant, positive RWS anomalies north of the Caribbean can be found in both panels. These are also accompanied by a downstream trough (Fig.

4.8a). Although being slightly weaker and of smaller spatial extent, significant SEA related source activity can be found basically in the same places (Fig. 4.9b). This co-location of SEA and CPPD related RWS activity and the consistency with the wave train are strong indicators of a tropical-extratropical teleconnection.

4.2.3 Rossby wave propagation in the summer northern hemisphere

Next, we attempt to confirm the previously proposed pathways for Rossby wave propagation associated with the CPPD and the SEA. In chapter 1, we briefly introduced the basis for horizontal and vertical planetary wave propagation in a zonal mean background flow pointing out that easterly winds do not support the existence of stationary Rossby waves. Thus, any RWS inside the zone of JJA mean tropical easterlies that we identified previously (Fig. 4.9) is unlikely to be connected to Rossby waves propagating into the extratropics. As an indicator for possible pathways of stationary Rossby waves, we consider the stationary wave number K_S (Hoskins and Ambrizzi, 1993) which is calculated as in section 2.2.7. Apart from the background wind, this measure also takes into account the meridional gradient of absolute vorticity. The climatological JJA average of K_S is shown in Fig. 4.10. Regions where K_S has a finite local maximum can act as wave guides for stationary Rossby waves. In the hatched areas of Fig. 4.10, K_S is imaginary due to negative absolute vorticity gradients. These regions act as reflecting surfaces. White regions without hatching mark the critical layers where the zonal wind is easterly and nonlinear wave breaking occurs (Li et al., 2015).

With this in mind, it cannot be entirely ruled out that there is an influence from the Beaufort Sea on parts of the NAE sector. There is a window over the Hudson Bay that could allow propagation of Rossby waves out of the Arctic. However, K_S is quite small there allowing only very long waves to propagate. It is difficult to

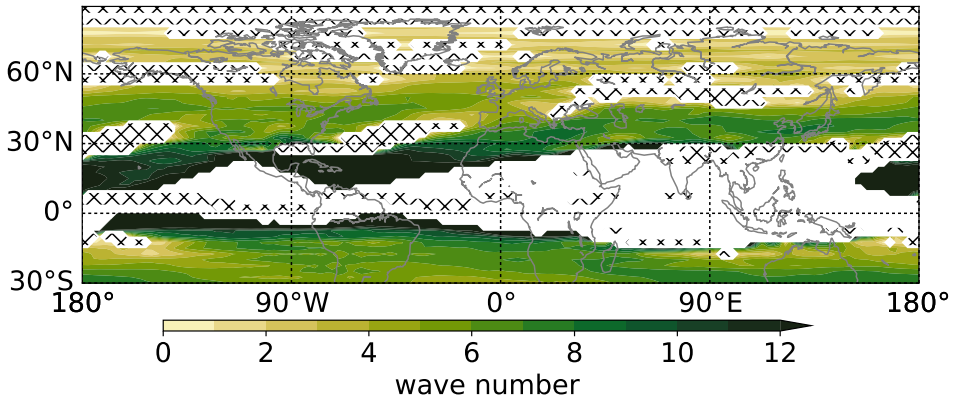

FIGURE 4.10: JJA climatological mean stationary wave number K_S. Shading shows K_S where it is real. In white areas, the wave number is imaginary due to easterly winds, while in the hatched regions this is due to the negative absolute vorticity gradient. The wave number is given in wavelengths per latitude band.

identify a local maximum that is suggestive of a wave guide. Additionally, the polar RWS associated with the SEA is located even further north where the weak planetary vorticity gradient does not support planetary wave propagation (compare Fig. 4.9 and 4.10).

Extending north-eastward from north of the Caribbean into the North Atlantic is a structure that is reminiscent of a wave guide with wave number 6. We want to point out that in both panels of Fig. 4.9 in the region north of the Caribbean, RWS activity could also be found even though being not statistically significant. It is conceivable that this is connected to convective activity further equatorward, i.e. inside the Caribbean part of the CPPD. Fig. 4.10 shows that there exists a pathway for planetary waves to propagate from this source region into the NAE sector.

For the most pronounced RWS in the eastern North Pacific, a connection to the NAE region is also possible. There is a weak wave guide over the North American continent that extends into the much more pronounced wave guide over the North Atlantic. This shows that the background flow field generally supports the propagation of planetary waves of wave number 5 between the Pacific and the NAE region.

4.3 Discussion

4.3.1 Is there a remote forcing of the SNAO?

Interannual SNAO variability

From the results of the relaxation experiments, only the Arctic and the stratosphere could not be entirely ruled out to contain a forcing of interannual SNAO variability (see Fig. 4.3) and we want to briefly discuss the plausibility of these links.

In case of the stratosphere, it is not obvious that there can be a forcing of summer variability from this part of the atmosphere at all. The winter NAO has been shown to be influenced by the anomalous stratospheric circulation through a top-down mechanism (Baldwin and Dunkerton, 1999; Baldwin and Dunkerton, 2001). Ineson and Scaife (2009) showed that it is also an important pathway through which tropical signals can propagate and exert a downward influence in the extratropics. However, these mechanisms rely on the possibility of planetary waves to propagate into the stratosphere. In the boreal summer season, easterly winds prevail in the stratosphere (Fig. A.5). Following the arguments of Charney and Drazin (1961), vertical propagation of planetary waves into the stratosphere is not possible under these circumstances. This theoretical limitation reduces our confidence in the skill of CLIM-STRA-NH in simulating the SNAO. Additionally, the skill of CLIM-STRA-NH is lower when we consider monthly SNAO anomalies, challenging the reliability of these results.

We want to point out that despite the limitation for planetary wave propagation into the stratosphere, there there could theoretically be a real influence from the stratosphere on the extratropical summer troposphere. Since the Rossby waves

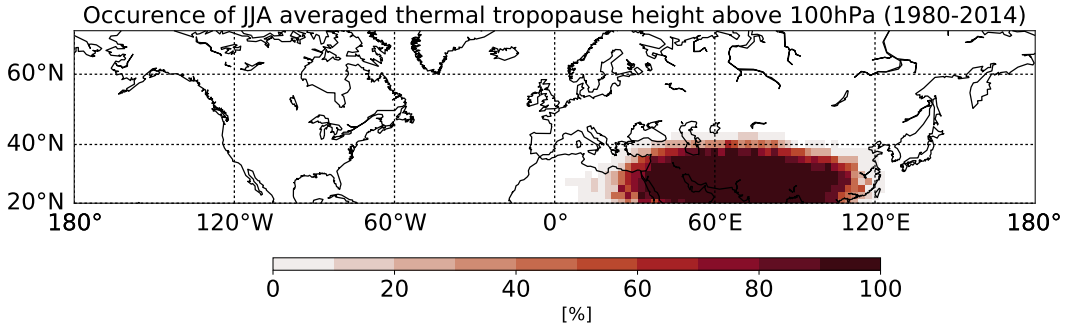

FIGURE 4.11: Frequency of occurrence of JJA mean thermal tropopause height above 100 hPa from ERA-Interim (1980-2014). In the white region, the tropopause height is never above 100 hPa in the analysis period.

cannot propagate into the stratosphere they either have to be dissipated or reflected as the zonal flow approaches 0 with height. The latter process is called downward wave coupling and has been shown to be an influence in the winter to spring northern hemisphere (Shaw et al., 2010). It is possible that both mechanisms also influence the summer troposphere. By prescribing a realistic stratospheric circulation, the reflection and dissipation of Rossby waves could be represented more realistically. If this process were at work, it could explain the better performance of the CLIM-STRA-NH experiment. However, this is highly speculative and can be supported by neither our results nor other studies.

Seeking to explain why the stratospheric relaxation experiments show the highest skill in simulating interannual SNAO variability, we examined the design of this experiment more closely and found that there can be an overlap between the transition zone of the relaxation region in CLIM-STRA-NH (centred around approximately 50 hPa) and the troposphere. In Fig. 4.11, it is shown how often out of the 35 considered summers, a JJA mean thermal tropopause[3] above 100 hPa was observed in ERA-Interim. It is clear from this figure that even in the seasonal mean, tropopause heights in a large region from 20°N - 40°N and 20°E - 120°E are almost constantly above 100 hPa. In case the relaxation region and the troposphere overlap, we cannot be sure whether the observed skill arises from prescribing the stratospheric state or rather from prescribing part of the circulation of the extratropical troposphere. In fact, the reason for the high tropopause in this region is likely to be the strong convective activity associated with the Indian Summer Monsoon (ISM). There is evidence that summer variability in the NAE sector is influenced by planetary waves generated by the strong diabatic heating anomalies associated with the ISM (Lin and Wu, 2012). Thus, it is possible that the stratospheric relaxation experiment actually shows skill arising from the diabatic forcing of the ISM. Since a stratospheric influence is questionable, we attribute the skill of CLIM-STRA-NH in simulating the SNAO to the overlap of the troposphere and the relaxation region.

[3]The height of the thermal tropopause was calculated using the algorithm of Reichler et al. (2003).

For the Arctic, an influence onto the SNAO cannot generally be ruled out. For instance, Cohen et al. (2014) discuss how changes in Arctic sea ice and snow cover can potentially influence the storm tracks, the jet stream and planetary waves in the mid-latitudes. While they focus on the winter season, they also point out that increased summer geopotential height anomalies over Greenland that project onto the negative SNAO phase were observed along with record low sea ice in 2007-2012. Screen (2013) relates the six wetter than average summers during that same period to a southward displacement of the jet stream consistent with a more negative SNAO[4]. By prescribing a sea ice forcing in an atmospheric model, they show that a reduction in Arctic sea ice favours the negative SNAO configuration much like the one they observe. Thus, Arctic sea ice and snow cover have the potential to influence the boreal summer extratropical circulation but it is beyond the scope of this thesis to analyse to what extent this is the case. Keeping in mind that there is some overlap between the Arctic relaxation region and the NAE sector, the skill of CLIM-ARC in simulating the SNAO is rather low. In the context of our experiments, we argue that there is no significant remote forcing of interannual SNAO variability over the ERA-Interim period.

Long-term SNAO variability

It became clear from Fig. 4.4 that all experiments fail to reproduce the observed negative trend of the SNAO but at the same time suggest that it is unlikely to be purely internal variability. We want to elaborate further on this issue.

The observed negative trend is consistent with the results of Knight et al. (2006) who use a 500 year simulation of the Hadley Centre Coupled Model (HadCM3) to show that during the positive phase of the AMV a cyclonic anomaly in slp over the British Isles is prevalent. This corresponds to the negative phase of the SNAO. The AMV-SNAO link is supported by Sutton and Hodson (2005) who compute the observed composite difference in slp between one positive and one negative AMV phase and recover the negative SNAO pattern. Since the AMV is mostly in an upward/warming phase during the ERA-Interim period (1980-2014), a negative SNAO trend is consistent with the aforementioned studies. We confirm this by regressing 8-year running means of ERA-Interim z_{500} anomalies onto the AMV index, shown in Fig. 4.12. The pattern of the negative SNAO clearly arises in the NAE sector but it should be stressed that by computing an 8-year running mean we decrease the number of degrees of freedom and reduce the length of the time series that are correlated from 32 to 25 years[5]. In this context, the positive trend in CET (Fig. 3.12) can also be understood. Even though the SNAO forces a large part of the interannual surface temperature variability, on multidecadal time scales both respond to the forcing of the AMV. While the AMV is negatively correlated with the SNAO, it

[4]Note that we also find the SNAO to be in its negative phase during these years except in 2010 when it is weakly positive, see Fig. 3.1.

[5]The AMV index is only available until 2011.

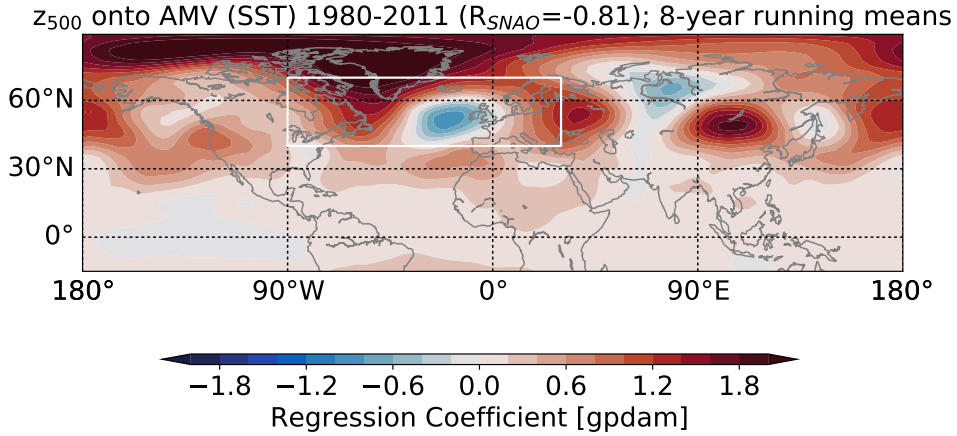

FIGURE 4.12: Regression of an 8-year running mean of z_{500} (ERA-Interim) onto an 8-year running mean of the AMV index calculated from the Kaplan SST dataset (available at `https://www.esrl.noaa.gov/psd/data/timeseries/AMO/`, see Enfield et al., 2001). White box marks the NAE region.

is positively correlated with surface temperature. Thus, the observed positive CET trend is consistent with the upward AMV phase. Despite the evidence from the regression analysis (Fig. 4.12) and the literature we want to point out that not all of our results regarding the link between the AMV and the SNAO fully support this. First, the relaxation experiments with prescribed SST/SI are highly unlikely to simulate a negative SNAO trend. Second, when no detrending is done prior to computing the regression of SST onto the SNAO index, the SST pattern that results does not resemble the AMV imprint (Fig. A.6). Hence, we conclude that further investigation of the AMV-SNAO link is necessary but beyond the scope of this thesis, mostly because the data of 35 years used here is not sufficient to analyse a multidecadal phenomenon.

4.3.2 Is the SEA remotely forced?

In the previous sections, the potential for successfully predicting the SEA mode turned out to be higher than for predicting the SNAO. There is a robust link of the mode with a dipole of convective activity between the Caribbean and the tropical central Pacific and we were able to show that this dipole is associated with a Rossby wave train that originates in the eastern North Pacific generating the SEA pattern in the NAE sector. In the following, we want to discuss this teleconnection and relate it to previous studies.

As mentioned above, the SEA pattern has been rarely discussed in the existing literature. However, the authors of a number of studies on the summers of 2003 and 2015 find the extreme European temperatures and dryness during these years to be related to a large-scale circulation anomaly that bears strong resemblance to the negative SEA phase (Black et al., 2004; Douville et al., 2011; Duchez et al., 2016). To our knowledge, Cassou et al. (2005) are the only authors that have identified this structure as a recurring summer weather regime. Like in the case studies however,

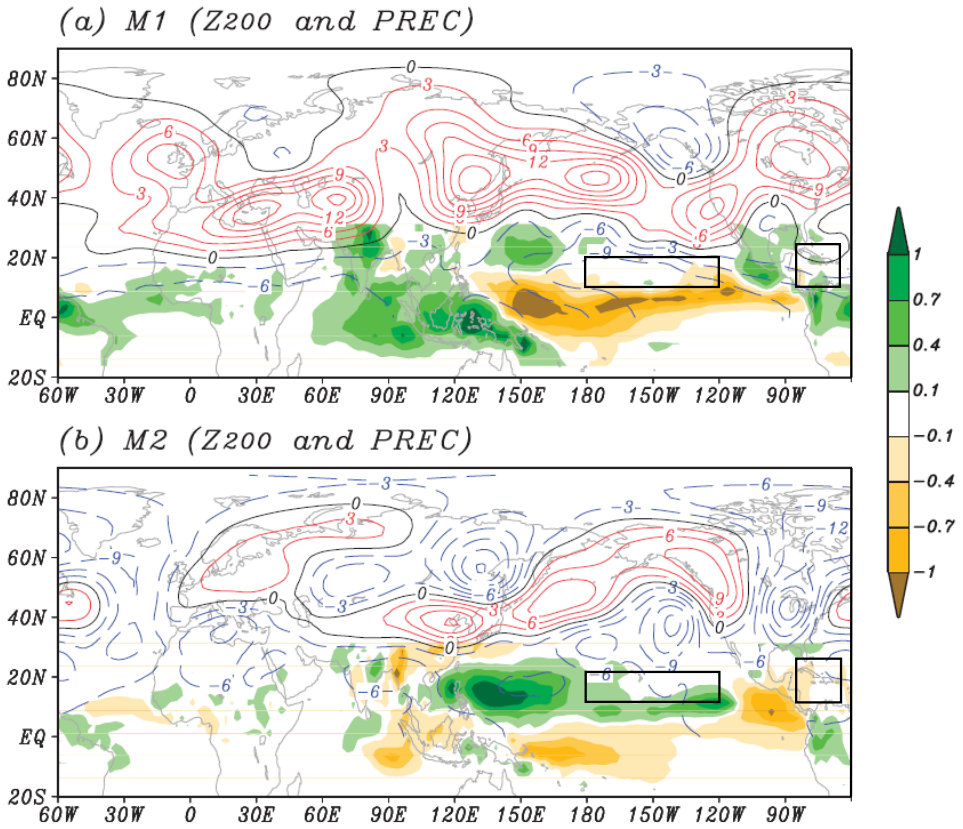

FIGURE 4.13: Modified Fig. 2 from Ding et al. (2011). The first (a, M1) and second (b, M2) mode of an MCA of JJA northern hemisphere z_{200} (contours, interval 3 m) and tropical (15°S-30°N) precipitation (shading, interval 0.3 mm day^{-1}). z_{200} is obtained from the NCEP-NCAR reanalysis, precipitation from the National Oceanic and Atmospheric Administration's (NOAA) global monthly precipitation reconstruction.The patterns show the anomalies associated with one standard deviation in time series of the expansion coefficient of the MCA. The black boxes were added for reference and indicate the approximate locations of the CPPD boxes.

they only find the negative SEA phase (see Fig. 3.10b) to be of relevance. They also study the European heat wave of 2003 and show that it was associated with the occurrence of this regime in June. Using observed outgoing longwave radiation anomalies, they further argue that it was related to significant, positive precipitation anomalies in the Caribbean (see also Douville et al., 2011). Note that this is contrary to our finding that the negative SEA phase is accompanied by below normal precipitation in the Caribbean part of the CPPD. To resolve this contradiction, it would be necessary to study the CPPD-SEA relationship on a monthly basis. Furthermore, considering several occurrences of strong SEA phases as opposed to just one case as in the aforementioned studies is necessary to resolve the nature of the relationship.

We found the SEA mode to be the NAE manifestation of a zonal wave number 5 stationary wave train that is generated in the eastern North Pacific. There, its source is caused by upper level divergence as a response to a convective precipitation in the

CPPD. As pointed out before, Ding et al. (2011) find the Circumglobal Teleconnection (CGT) - also a zonal wave number 5 pattern - to be the dominant teleconnection in the summer northern hemisphere. It is displayed for reference in Fig. 4.13a. Apart from having the same wave number, the two patterns do not resemble each other. The second most dominant pattern is the western Pacific-North America (WPNA) pattern (Ding et al., 2011) and is shown in Fig. 4.13b. Although this wave train lacks a pronounced anomaly where the main centre of action of the SEA is located, its negative phase strongly resembles our CPPD wave train. The similarity is especially pronounced over the eastern North Pacific and the North American continent.

Ding et al. (2011) find the WPNA to be forced by the diabatic heating anomalies over the Philippine Sea that accompany the western North Pacific summer monsoon (WNPSM). The precipitation anomalies associated with the teleconnection patterns are shown by the shading in Fig. 4.13. In fact, these relates well to the precipitation anomalies north of the equator associated with the SEA index (Fig. 3.9). The interannual variability of the WNPSM[6] is highly correlated with the interannual East Asian summer monsoon (EASM) variability (Ding et al., 2016). A measure for the EASM variability is the index of the Pacific-Japan (PJ) pattern (Sun et al., 2010). Attempting to test whether the CPPD wave train is also influenced by the WNPSM, we calculate the correlation between the CPPD and the PJ index. If such a link exists, the indices should be positively correlated. This is because the negative PJ pattern is connected to the WNPSM (Wang et al., 2001) and thus the positive phase of the WPNA while the CPPD is associated with a wave train that resembles the negative WPNA phase. Indeed, the correlation is found to be weakly positive (0.26). The PJ index is also weakly correlated with the SEA index (0.30). Both correlations are not statistically significant and are not sufficient to provide evidence for a relationship between the CPPD wave train and the WNPSM. To further test the link, we regress z_{500} anomalies onto the PJ index (Fig. 4.14a). Even though most extratropical anomalies away from the PJ region are not significant, we find the pattern that arises to be consistent with the CPPD wave train and the negative WPNA phase. Hence, the CPPD wave train appears to be weakly influenced by the WNPSM but the main forcing is through rainfall anomalies in the Caribbean and tropical Pacific.

On top of being associated with rainfall anomalies in the Philippine Sea, the WPNA is accompanied by a precipitation dipole between the central tropical Pacific and Mexico, much like the CPPD whose boxes are indicated in Fig. 4.13. However, also the CGT is accompanied by weak precipitation anomalies of opposing signs in these areas. By correlating northern hemisphere z_{200} with precipitation over Mexico, Ding et al. (2011) argue that there is an influence of the Mexican monsoon on the CGT. We find the resulting correlation pattern (their Fig. 9c) to also carry some characteristics of our CPPD wave train, especially over North America. As both the CGT and the WPNA are associated with a precipitation dipole between the Caribbean and the tropical Pacific (Fig. 4.13), it could be difficult to separate these two modes

[6]Measured by the WF (Wang and Fan) index (Wang and Fan, 1999)

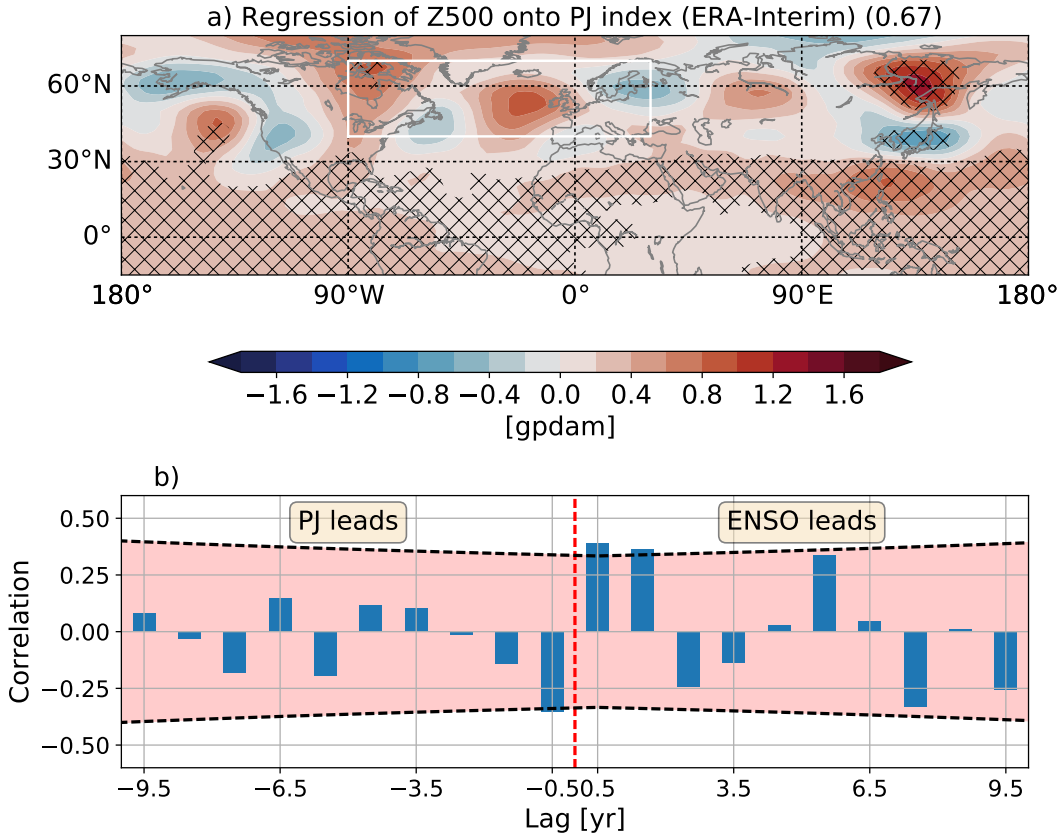

FIGURE 4.14: a) As in Fig. 4.8 but for ERA-Interim JJA mean z_{500} regressed onto the PJ index. Number in parentheses in the title is the pattern correlation between the observed SEA pattern and the regression pattern in the NAE sector (indicated by the white box). b) Lead/lag correlations between JJA mean PJ and DJF mean Niño 3.4 index. Correlations that fall outside the red envelope are statistically significant at the 95% level.

using just the CPPD. It is possible that our CPPD wave train is actually a manifestation of a simultaneous occurrence of both patterns. The tight link with the SEA could point to the fact that the SEA pattern is forced when the opposing phases of the CGT and the WPNA coincide.

The CGT and the WPNA have been shown to be linked to developing and decaying ENSO events respectively (Ding et al., 2011). Because the CPPD regions lie in the immediate vicinity of the strongest ENSO related anomalies, we test a possible link between these two. It should be noted that all relationships that were shown above hold equally well when a simultaneous ENSO signal (e.g. the JJA Niño 3.4 SST index) is linearly removed (not shown). This points to a negligible instantaneous ENSO influence. However, in the boreal summer season, the ENSO signal is weakest. It is possible that there is a lagged influence that only becomes evident when considering the relationship between the CPPD and a measure of winter (DJF) ENSO activity. In Fig. 4.15, we show the lagged correlation between the JJA CPPD and the DJF Niño 3.4 SST index. The maximum correlation is found when the CPPD leads by a half year and is negative, indicating that positive CPPD anomalies are

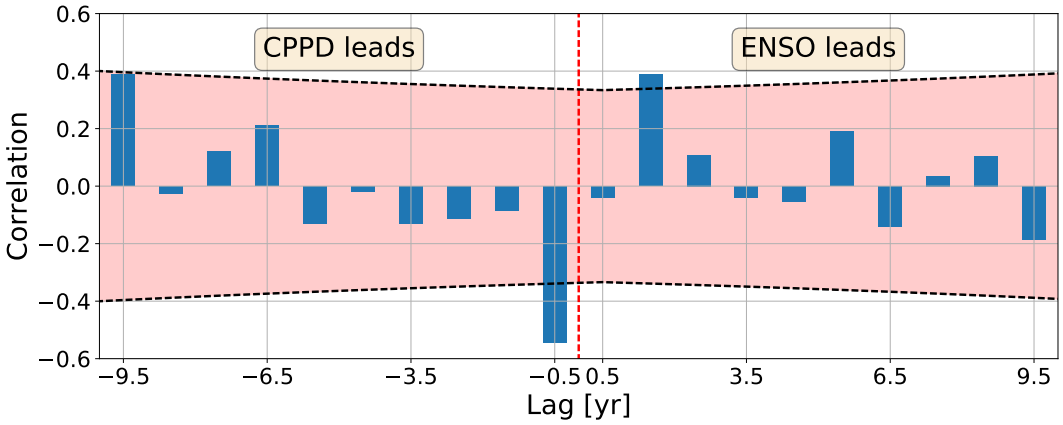

FIGURE 4.15: Lead/lag correlation between the JJA mean CPPD and the DJF mean Niño 3.4 SST index. Correlations that fall outside the red envelope are statistically significant at the 95% level.

associated with developing La Niña events. This is surprising when we consider that the CPPD wave train is similar to the negative WPNA phase which has been shown to occur in summers after a peak El Niño winter (Ding et al., 2011). Trying to confirm the relationship of the WPNA with the ENSO cycle, we calculate lead/lag correlations between DJF ENSO and the JJA PJ index as a measure of the strength of the negative WPNA phase (Fig. 4.14b). The PJ index is most strongly correlated with the developing ENSO phase confirming that the WPNA follows peak La Niña events. Clearly however, the PJ index is also significantly correlated with ENSO at lags -0.5 yrs and 1.5 yrs which confirms the results of Fig. 4.15.

Some of the results presented above contradict the findings of Ding et al. (2011) concerning the WPNA teleconnection. It is conceivable that the different definition of the CPPD teleconnection leads to these discrepancies. The use of different data products and the different analysis period are also possible contributors. In general however, it is evident that the CPPD wave train, and the SEA as its NAE part, are closely linked to the WPNA.

4.3.3 Why do tropical relaxation experiments fail at reproducing the SEA?

In the previous sections, it became clear that the relaxation of the tropical atmosphere degrades the model's ability to simulate the SEA mode. Considering the evidence for a tropical-extratropical teleconnection associated with the SEA, this is surprising. It also stands in marked contrast to the results of Douville et al. (2011) who show that the representation of the stationary waves in the northern hemisphere summer benefits from relaxation in the tropics. Here, the reasons for the failure of the tropical relaxation experiments will be discussed.

We have collected evidence for precipitation in the CPPD driving a significant part of the SEA mode. The CPPD boxes lie between 10°N and 25°N, i.e. they are located inside the tropical relaxation zones. As a consequence, CLIM-TROPICS and

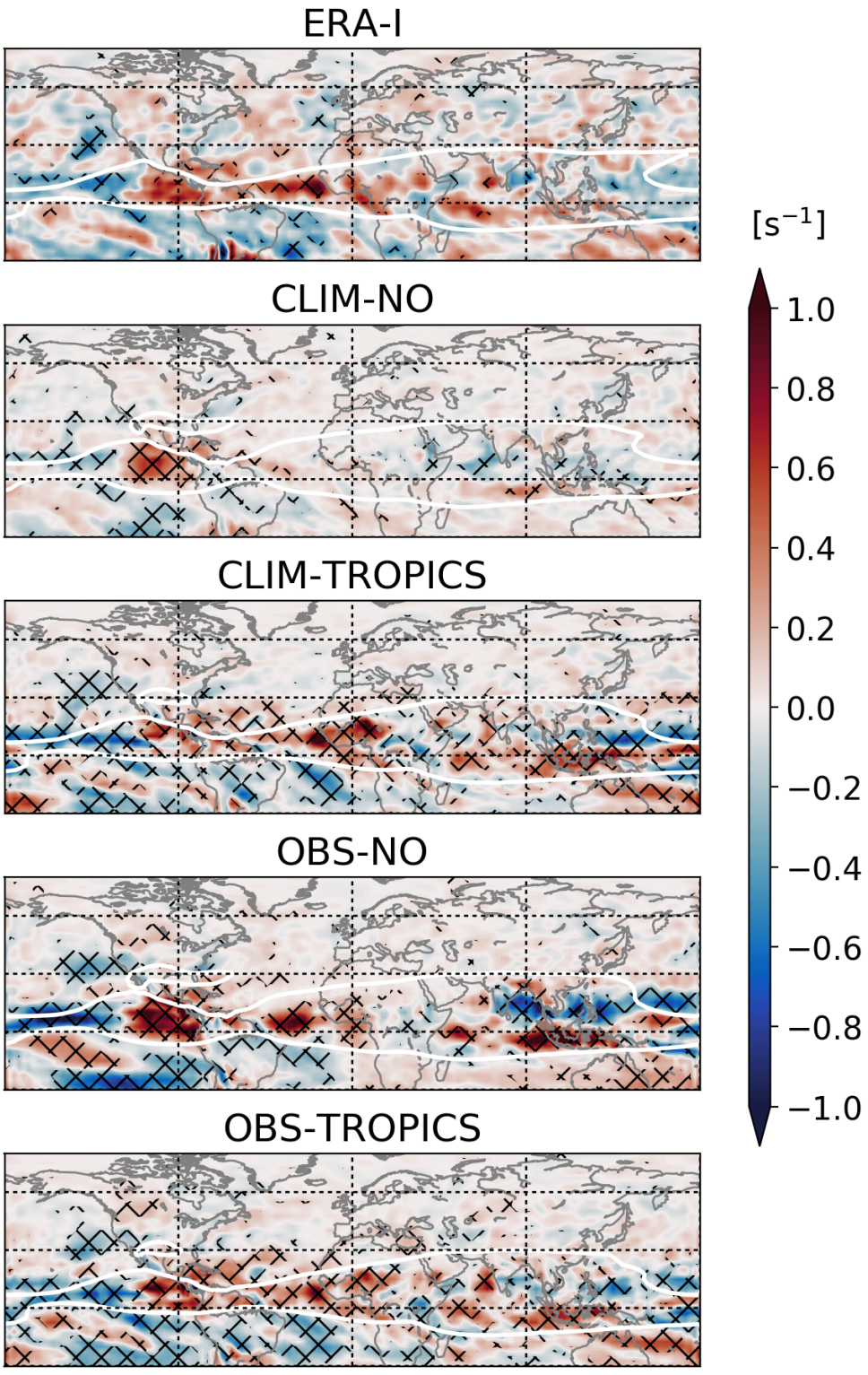

FIGURE 4.16: Regression of the JJA mean divergence at 200 hPa onto the CPPD in units of s^{-1} per standard deviation in CPPD index. Red colour for divergence and blue for convergence of flow. For the top panel, winds and precipitation from ERA-Interim were used, for the remaining panels data from all ensemble members of respective experiment as indicated in the title was used. Hatching indicates where the regression coefficients are statistically significant. White line marks the climatological mean zero-wind line of the respective dataset.

OBS-TROPICS simulate the CPPD precipitation well. Since convergence in the mid-latitudes as a consequence of convection in the tropics is a main contributor to the RWS, we consider the divergence at 200 hPa related to the CPPD index in Fig. 4.16. All model ensembles reproduce the divergence over the eastern tropical Pacific and the Caribbean and the convergent flow over the central Pacific. This is to be expected since the divergence/convergence anomalies are physically linked to convective precipitation anomalies in the tropics. All of the experiments also capture the convergence around 30°N. This convergence is the dominant contributor to the RWS that is associated with the CPPD. While it is very weak in CLIM-NO, it is of similar magnitude in CLIM-TROPICS, OBS-NO and OBS-TROPICS. Clearly, the failure of the tropical relaxation experiments at reproducing the SEA pattern does not lie in the generation of the planetary wave train. This is confirmed by the tropical relaxation experiments being able to simulate the observed wave train response to the CPPD forcing over the North Pacific and North America (Fig. 4.8). Additionally, the stationary wave number in all experiments is very similar to ERA-Interim (Fig. A.7). However, the signal gets strongly disturbed in CLIM-TROPICS and OBS-TROPICS the further we move eastwards, i.e. downstream of the source region. The wave train in these experiments appears to move south-eastward over eastern Canada and then to vanish towards the tropics. This happens neither in ERA-Interim nor in the experiments without relaxation. In both, the wave train is reflected back towards Europe. We hypothesize that the relaxation of the tropical atmosphere leads to enhanced dissipation inside the relaxation zone. Since it is the only difference between the successful OBS-NO ensemble and the failing OBS-TROPICS ensemble, it must be the relaxation itself that causes the wave train to be altered.

5 Concluding remarks and outlook

As it is the dynamically more active season, most studies of large-scale climate variability have been conducted for winter. The dominant mode of atmospheric winter variability in the NAE sector, the NAO, explains up to 36% of seasonal slp variance (Hurrell et al., 2003) and strongly determines winds, temperatures, and precipitation in the region. There are indications that there also exist such large-scale modes of variability in summer (Barnston and Livezey, 1987) and that these are accompanied by characteristic anomalies in surface climate variables (Folland et al., 2009). In this thesis, we have examined the summer circulation of the atmosphere in the NAE region with a focus on the impacts of the characteristic large-scale modes. Furthermore, influences from remote regions on these modes have been investigated and discussed in terms of their potential for improved prediction of the seasonal summer variability. In the following, we summarise the main findings of our study and give some perspective for future work.

5.1 Characteristics of the SNAO and the SEA

5.1.1 The SNAO mode

Like Folland et al. (2009) have done previously, we have shown the existence of a distinct mode of interannual geopotential height variability that is the summer counterpart to the winter NAO. It is defined as the first EOF of JJA mean z_{500} anomalies over the NAE region (40°N to 70°N and 90°W to 30°E) and explains 36% of JJA z_{500} variance. This amount of explained variance is comparable to the winter NAO. Like its winter equivalent, the summer NAO (SNAO) is associated with changes in the zonal wind component. However, while the winter NAO is characterised by a strictly meridional dipole in atmospheric mass between Iceland and the Azores, the centres of action of the SNAO are located west of southern Greenland and over the British Isles. Thus, both phases of the SNAO are also accompanied by anomalies in the geostrophic part of the meridional wind and a meandering of the jet.

We have shown that the SNAO is accompanied by significant temperature and precipitation anomalies in the NAE region. The main surface characteristics of the positive SNAO phase are warm and dry anomalies over the British Isles, Scandinavia and north-western continental Europe and warm anomalies over eastern North America. Southern Europe and the Mediterranean region are governed by

weakly cool and wet anomalies. West of Greenland, cold and wet anomalies prevail while to its south-east warm and wet anomalies are associated with the positive SNAO. Like its winter equivalent, the SNAO controls temperatures via anomalies in temperature advection. A second driver of temperature anomalies are large-scale rising and sinking motions in the main centres of action. These are associated with cloud cover anomalies and thus influence the amount of solar radiation reaching the surface (Folland et al., 2009). The enhanced/suppressed cloud formation associated with the second mechanism also explains the main precipitation anomalies within the NAE sector but advection of moisture can be an additional cause for the SNAO related precipitation pattern. A quantification of the contribution of the processes driving the surface anomalies could be gained for example by analysing advection, cloud cover, and turbulent heat fluxes related to the SNAO. However, especially concerning the latter two, the lack of reliable data can be problematic.

5.1.2 The SEA mode

Additional to the SNAO, another mode of summer variability could be identified. This is the summer East Atlantic (SEA) mode which is defined as the second EOF of JJA mean z_{500} anomalies over the NAE region and explains another 18% of JJA z_{500} variance. It is characterised by one main centre of action over the northern East Atlantic and a much weaker centre of opposite sign east of it. Its associated circulation anomalies are mainly meridional. In fact, it is the NAE part of a wave train along the climatological summer mean position of the northern hemisphere jet stream. In its positive phase, the SEA is reminiscent of a blocking pattern over the East Atlantic.

In the literature however, only the negative phase of the SEA has been addressed (Cassou et al., 2005) - an issue that needs closer inspection. A linear approach such as PCA will always return pairs of patterns that are symmetric. A second constraint of the PCA is the orthogonality of the modes. In this regard, it can be revealing to use a non-linear approach to overcome these constraints and more robustly identify the circulation regimes.

It has been shown that the SEA is also accompanied by significant anomalies in precipitation and temperature in the NAE region. The structure of the SEA related temperature anomalies is almost identical to the z_{500} pattern of the SEA itself. Over the eastern North Atlantic and Europe, significant dry/wet anomalies are co-located with positive/negative z_{500} and temperature anomalies. This indicates that the mechanism causing these is the reduced/enhanced cloud cover in regions of anomalous SEA related large-scale sinking/rising. Even though the SNAO related precipitation and temperature anomalies are found to be stronger, the SEA can also have a significant impact on the summer mean climate in Europe.

The most important influence of the SEA mode is perhaps on the likelihood of extreme temperatures in Europe. Several studies show that the summers of 2003

and 2015 that were accompanied by exceptionally high temperatures and dryness are related to a circulation anomaly over the northern East Atlantic (Cassou et al., 2005; Duchez et al., 2016). This anomaly clearly resembles the negative SEA phase. Due to the great socio-economic impacts of such extreme events, it is an issue for future studies to examine how the chances for temperatures and precipitation in the tails of their summer distributions change under the SEA regime.

5.2 Potential drivers of summer variability

The second aim of this thesis was to find potential for the predictability of the summer variability in the NAE sector with a focus on the modes described above. For this purpose, seasonal ensemble hindcast experiments have been carried out with an atmospheric general circulation model. In these experiments, we have applied a relaxation technique in different specified regions of the atmosphere in order to identify possible forcings from these regions. As a first guess for remote influences however, we have considered correlations between the summer variability modes and other climate variables external to the NAE atmosphere. In this case, external can also refer to an oceanic variable such as SST inside the NAE sector.

An indicator for influences that offer potential for an improved prediction are the correlations of the SNAO/SEA with SST. It was found that the SNAO and the SEA strongly co-vary with SST in the vicinity of the NAE region. The resulting patterns were interpreted mostly as a response to the anomalous circulation. However, since there is evidence for two-way interactions between the ocean and the atmosphere (Gastineau and Frankignoul, 2015), an analysis of lead-lag relationships between the monthly SST and SNAO/SEA could give insights into the nature of this relationship. A forcing from a slowly-varying component such as the ocean bears some potential for an improved prediction.

Similarly, lead-lag correlation analysis of the monthly SNAO/SEA and climate variables outside of the NAE region, e.g. in the tropics, could resolve whether the correlations between their seasonal means (chapter 3) actually represent forcings from these regions.

Using the relaxation experiments, it could be shown that relaxing the tropical atmosphere does not increase the skill in simulating the SNAO. The most successful experiments were those that relax either the stratosphere or the Arctic troposphere. However, we argued that the stratosphere is not a likely candidate since the propagation of planetary waves in the summer stratosphere is strongly inhibited by the predominance of easterly winds. We reasoned that the skill of the stratospheric relaxation experiments actually comes from the overlap of the relaxation region with the troposphere in the region where the Indian summer monsoon (ISM) is located. Since the ISM has been linked to NAE summer variability before (Lin and Wu, 2012), further investigation of this possible tropical-extratropical pathway could reveal potential for the prediction of the SNAO.

Experiments in which the Arctic troposphere was relaxed exhibited the highest skill at reproducing the SNAO and there have been studies linking Arctic sea ice anomalies with the large-scale circulation in the NAE region (Cohen et al., 2014). Yet, due to the overlap of the relaxation region with the definition region of the SNAO, we could not interpret the skill of the Arctic relaxation experiment entirely as a consequence of a remote influence from the Arctic onto the SNAO. In fact, considering that there is some overlap, the skill is small. In order to be able to more carefully address an Arctic link, experiments with a clearer separation of the relaxation zone and the analysis domain need to be designed.

Although studies indicate that the long-term SNAO variability is linked to the Atlantic Multidecadal Variability (AMV) (Sutton and Hodson, 2005; Knight et al., 2006) and reanalysis data corroborates this relationship, our experiments using observed anomalies of SST/SI at the lower boundary did not show any skill at reproducing the weakly negative SNAO trend. Thus, we could not find any potential for predicting the leading mode of summer variability in the NAE region in our experiments. Of course, the available data for our analyses only covers 35 years. Certainly, the analysis of a multidecadal phenomenon requires much longer time series and is an issue for future work.

As for the SNAO, the potential for predicting the SEA has been examined using the same experiments. The only experiment that shows significant skill in predicting the observed evolution of the SEA did not use a relaxation but had observed anomalous instead of climatological SST/SI as lower boundary forcing. We collected further evidence from the reanalysis that the SEA mode is the NAE part of a tropical-extratropical teleconnection pattern. This is the most important result of this thesis. The teleconnection pattern is a wave train of zonal wave number 5. We were able to show that its origin lies in SST anomalies in the Caribbean and the tropical Pacific. There, the anomalous SSTs cause diabatic heating associated with the anomalous rainfall. This diabatic forcing results in upper level divergence anomalies above these regions which are balanced by anomalous divergence of the opposite sign in the eastern North Pacific. As a consequence, there is a Rossby wave source induced in the vicinity of the jet stream. This excites planetary waves that propagate downstream and set up the teleconnection pattern. This robust physical link between the tropical and the extratropical circulation offers potential for an improved prediction of the evolution of the SEA mode.

Additional to the influence forcing from the Caribbean and the tropical Pacific, we found this teleconnection to be also weakly influenced by the western North Pacific summer monsoon (WNPSM). This is in concert with a study by Ding et al. (2011) who find a boreal summer teleconnection pattern much like the one we identified and argue that this western Pacific-North America (WPNA) pattern is forced by the WNPSM. However, while they show that it occurs in summers following a peak ENSO event, we find indications for the wave train coinciding with the developing phase of ENSO. It is possible that the teleconnection we consider here is a mixture

of the two dominant teleconnection patterns that Ding et al. (2011) find. Thus, our results are only partly in agreement with previous work and this has to be resolved by further studies.

5.3 Failure of the tropical relaxation experiments at reproducing tropical-extratropical teleconnections

Since the main potential for predicting the SEA related circulation originates from rainfall anomalies in the tropics, we expected experiments with relaxation of the tropical atmosphere to perform best at simulating it. However, we find these experiments to have less skill at predicting the SEA than the ones without relaxation. We were able to show that the problem does not lie in the excitation of the planetary wave pattern - tropical relaxation experiments naturally predict precipitation very accurately and consequently generate the correct Rossby wave source. In fact, the characteristics of the wave train are strongly altered downstream of the source region. It is conceivable that the reason for the degradation of the forecast through the relaxation of the tropics comes from the different dissipation characteristics inside the relaxation zone. This result is in contrast to Douville et al. (2011) who find the simulation of the stationary waves in boreal summer to be improved by relaxation of the tropics. We conclude that, especially in the summer season when teleconnections are expected to be weaker than in winter, the relaxation technique might not be ideal in the study of planetary waves.

As the relaxation technique itself has been found to be an issue for the correct representation of planetary waves, it could be a task for future studies to design different relaxation experiments. For instance, applying a relaxation in the individual monsoon regions instead of the whole tropical sector could help to reduce the influence of spurious dissipation. This was done by Douville et al. (2011) but did not significantly change the results compared to relaxation of the whole tropical sector. We have shown that the excitation of the waves is well predicted by the tropical relaxation experiments but the wave train gets altered further downstream. Confining the relaxation zone zonally would reduce the area where the spurious dissipation occurs and could improve the performance of the hindcasts with relaxation. It would also allow to more clearly separate in which region a forcing has its origin. An alternative to the relaxation technique would be to force the hindcasts with diabatic heating anomalies that would have to be derived from precipitation data.

A Appendix

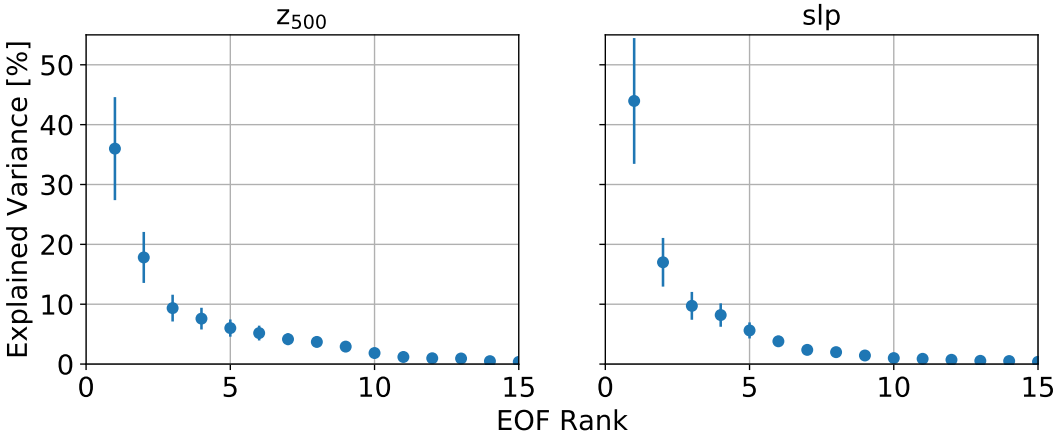

FIGURE A.1: Screeplots showing the explained variance fraction of the respective EOF for the first 15 EOFs of JJA mean z_{500} anomalies (left) and of JJA mean slp anomalies (right). Error bars shown are based on North's rule-of-thumb (North et al., 1982).

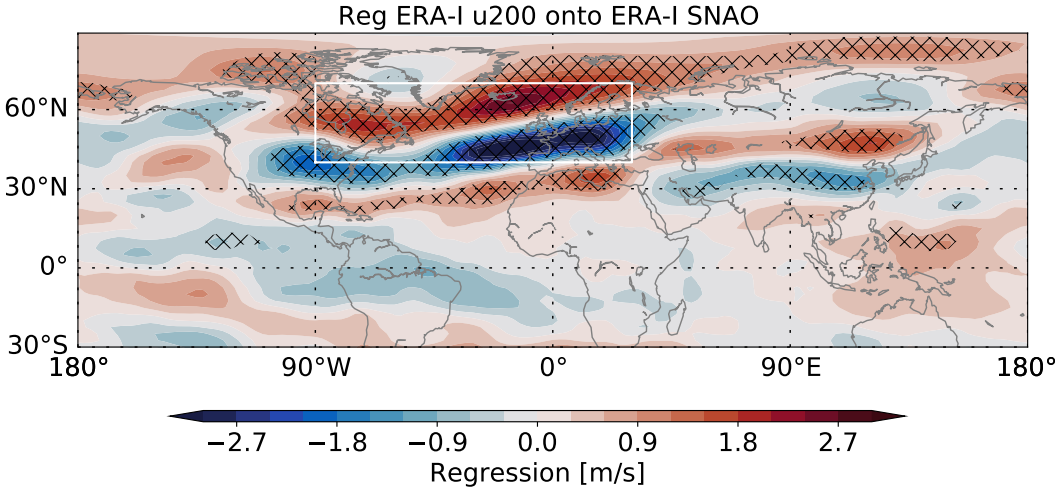

FIGURE A.2: Shading: regression of ERA-Interim detrended JJA mean zonal wind at 200 hPa (u_{200}) onto the detrended observed SNAO index in m s^{-1} per one standard deviation of the SNAO index. Hatching indicates where the regression coeffiecient is significantly different from zero on the 95% level. White box marks the NAE region over which the PCA has been conducted.

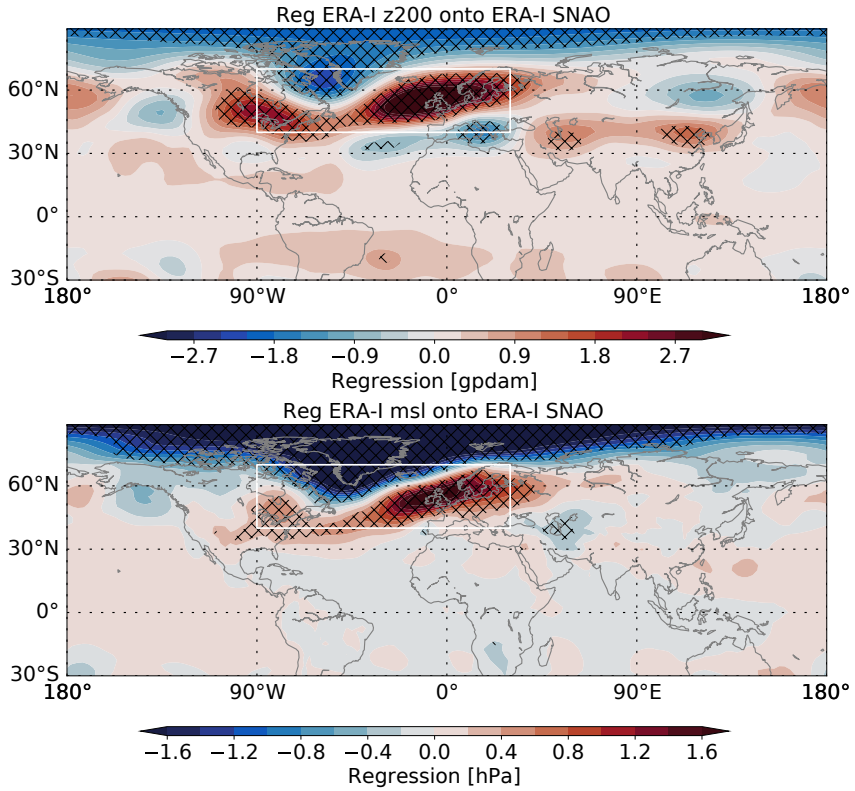

FIGURE A.3: As in Fig. A.2 but regressing detrended slp (bottom) and z_{200} (top) onto the detrended observed SNAO.

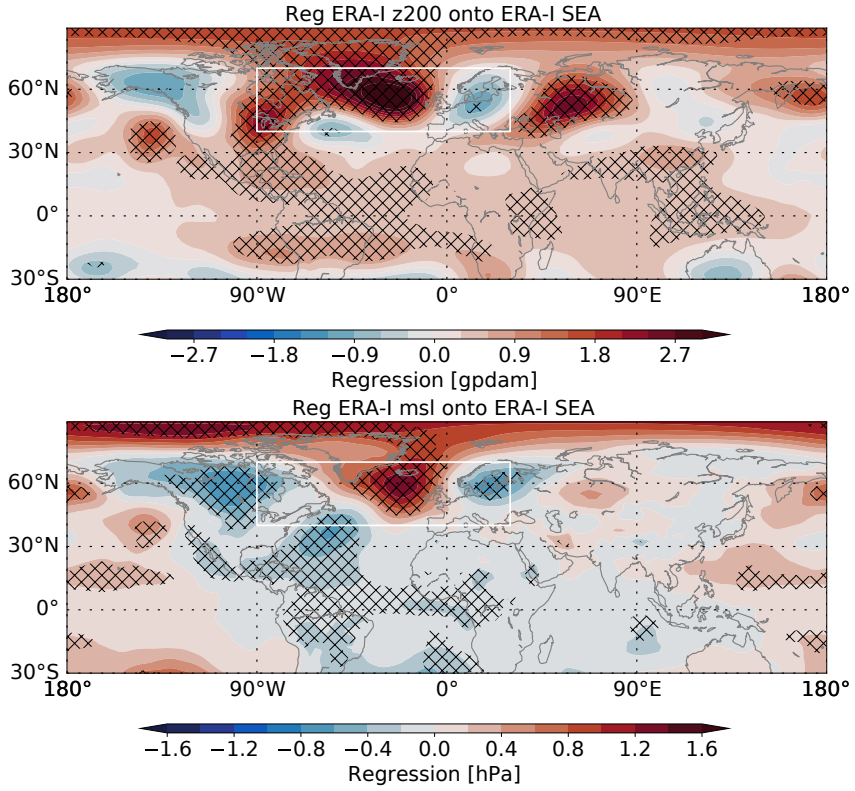

FIGURE A.4: As in Fig. A.3 but regressions onto the detrended observed SEA index.

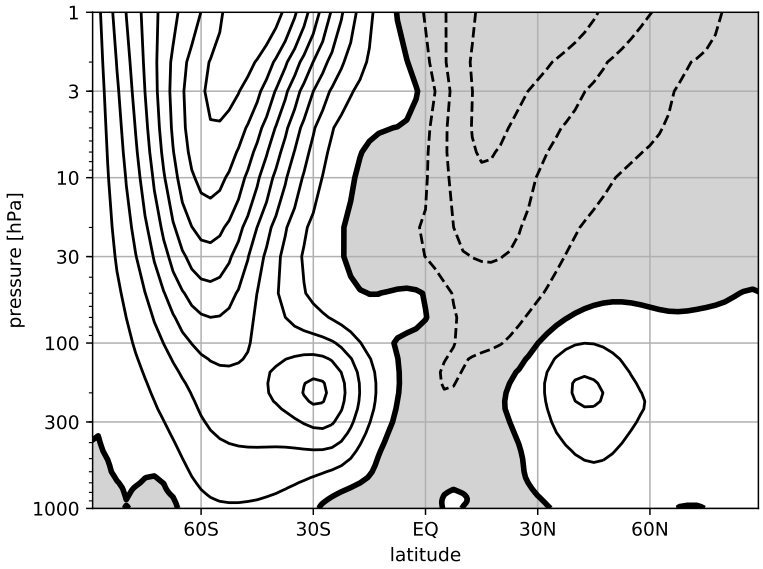

FIGURE A.5: Latitude-height section of ERA-Interim (1980-2014) JJA climatology of zonal mean zonal wind $\langle u \rangle$. Solid contours indicate positive (westerly) values; where $\langle u \rangle$ is negative (easterly) contours are dashed and background colour is grey; zero contour is thick; contour interval is 10 ms^{-1}.

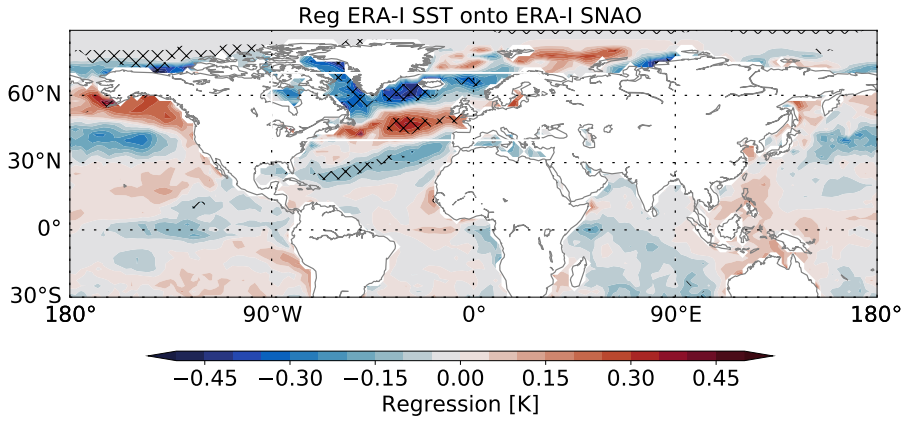

FIGURE A.6: As in Fig. 3.3 but here neither SST nor the SNAO have been detrended prior to regressing.

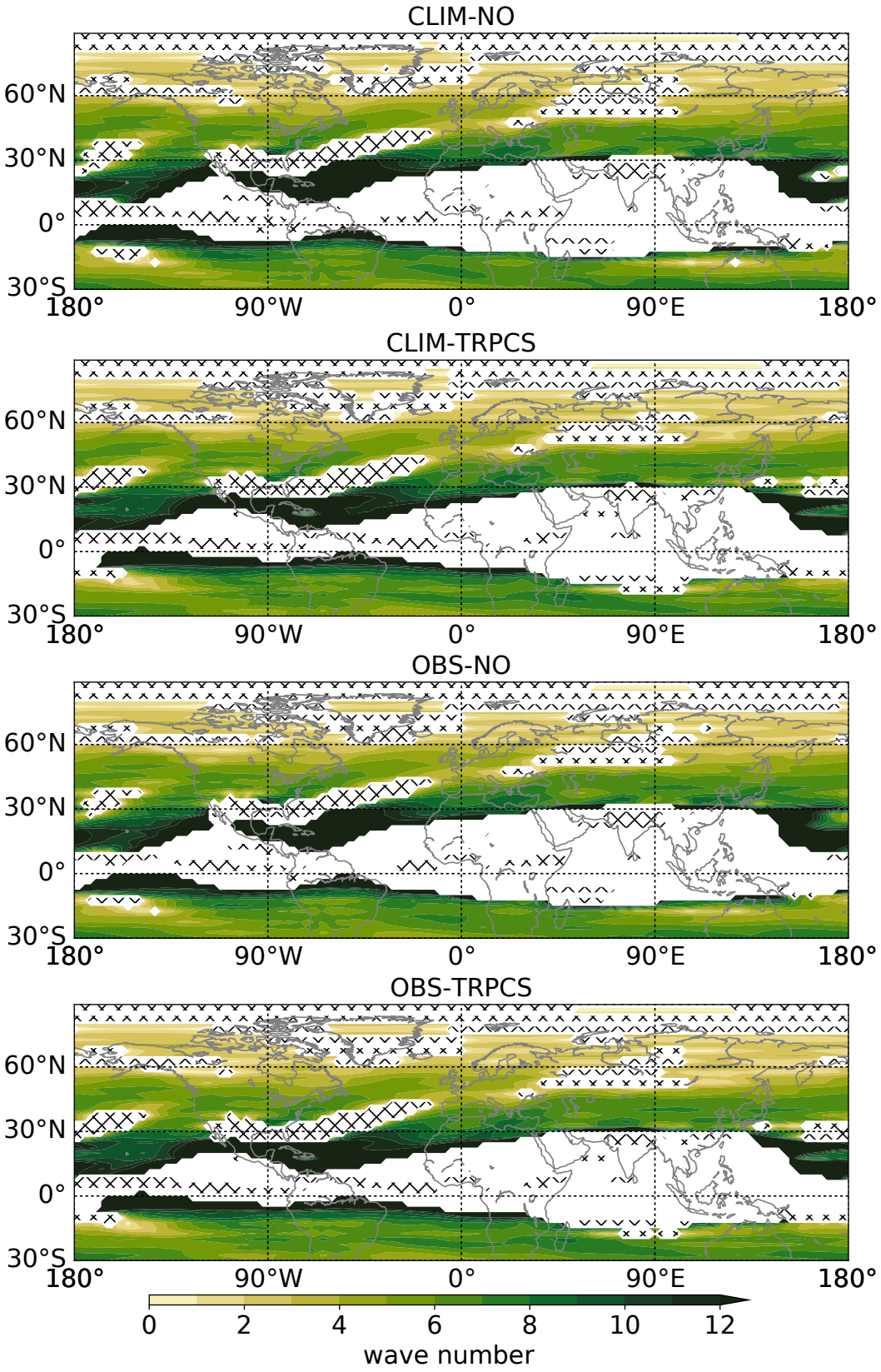

FIGURE A.7: As in Fig. 4.10 but computed from the ensemble mean u_{200} of the experiment indicated in the title of each panel.

Bibliography

Baldwin, M P and T J Dunkerton (1999). "Propagation of the Arctic Oscillation from the stratosphere to the troposphere". In: *Journal of Geophysical Research* 104 (D24), pp. 30,937–30,946. DOI: 10.1029/1999JD900445.

— (2001). "Stratospheric Harbingers of Anomalous Weather Regimes". In: *Science* 294, pp. 581–584. DOI: 10.1126/science.1063315.

Barnston, A G and R E Livezey (1987). "Classification, Seasonality and Persistence of Low-Frequency Atmospheric Circulation Patterns". In: *Monthly Weather Review* 115 (6), pp. 1083–1126. DOI: 10.1175/1520-0493.

Black, E, M Blackburn, G Harrison, B Hoskins, and J Methven (2004). "Factors contributing to the summer 2003 European heatwave". In: *Weather* 59 (8), pp. 217–223. DOI: 10.1256/wea.74.04.

Bladé, I, B Liebmann, D Fortuny, and G J van Oldenborgh (2012). "Observed and simulated impacts of the summer NAO in Europe: Implications for projected drying in the Mediterranean region". In: *Climate Dynamics* 39 (3), pp. 709–727. DOI: 10.1007/s00382-011-1195-x.

Branstator, G (2002). "Circumglobal Teleconnections, the Jet Stream Waveguide, and the North Atlantic Oscillation". In: *Journal of Climate* 15, pp. 1893–1910. DOI: 10.1175/1520-0442(2002)015<1893:CTTJSW>2.0.CO;2.

Cassou, C, L Terray, and A S Phillips (2005). "Tropical Atlantic influence on European heat waves". In: *Journal of Climate* 18 (15), pp. 2805–2811. DOI: 10.1175/JCLI3506.1.

Charney, J G and P G Drazin (1961). "Propagation of Planetary-Scale Disturbances from the Lower into the Upper Atmosphere". In: *Journal of Geophysical Research* 66 (1), pp. 83–108.

Charney, J G and J Shukla (1981). *Monsoon Dynamics*. Ed. by J Lighthill and R P Pearce. Cambridge University Press, Cambridge. Chap. Predictability of monsoon, pp. 99–109.

Cohen, J, J A Screen, J C Furtado, M Barlow, D Whittleston, D Coumou, J Francis, K Dethloff, D Entekhabi, J Overland, and J Jones (2014). "Recent Arctic amplification and extreme mid-latitude weather". In: *Nature Geoscience* 7 (9), pp. 627–637. DOI: 10.1038/ngeo2234.

Coumou, D and S Rahmstorf (2012). "A decade of weather extremes". In: *Nature Climate Change* 2 (7), pp. 491–496. DOI: 10.1038/nclimate1452.

Czaja, A and C Frankignoul (1999). "Influence of the North Atlantic SST on the atmospheric circulation". In: *Geophysical Research Letters* 26 (1), pp. 2969–2972. DOI: 10.1175/JCLI-D-14-00424.1.

Dawson, A (2016a). "eofs: A Library for EOF Analysis of Meteorological, Oceanographic, and Climate Data". In: *Journal of Open Research Software* 4, e14. DOI: 10.5334/jors.122.

— (2016b). "Windspharm: A High-Level Library for Global Wind Field Computations Using Spherical Harmonics". In: *Journal of Open Research Software* 4 (1). DOI: 10.5334/jors.129.

Dee, D P, S M Uppala, A J Simmons, P Berrisford, P Poli, S Kobayashi, U Andrae, M A Balmaseda, G Balsamo, P Bauer, P Bechtold, A C M Beljaars, L van de Berg, J Bidlot, N Bormann, C Delsol, R Dragani, M Fuentes, A J Geer, L Haimberger, S B Healy, H Hersbach, E V Hólm, L Isaksen, P Kållberg, M Köhler, M Matricardi, A P Mcnally, B M Monge-Sanz, J J Morcrette, B K Park, C Peubey, P de Rosnay, C Tavolato, J N Thépaut, and F Vitart (2011). "The ERA-Interim reanalysis: Configuration and performance of the data assimilation system". In: *Quarterly Journal of the Royal Meteorological Society* 137 (656), pp. 553–597. DOI: 10.1002/qj.828.

Ding, H, R J Greatbatch, H Lin, F Hansen, G Gollan, and T Jung (2016). "Austral winter external and internal atmospheric variability between 1980 and 2014". In: *Geophysical Research Letters* 43, pp. 2234–2239. DOI: 10.1002/2016GL067862.

Ding, Q and B Wang (2005). "Circumglobal teleconnection in the Northern Hemisphere summer". In: *Journal of Climate* 18, pp. 3483–3505. DOI: 10.1175/JCLI3473.1.

Ding, Q, B Wang, J M Wallace, and G Branstator (2011). "Tropical-extratropical teleconnections in boreal summer: Observed interannual variability". In: *Journal of Climate* 24 (7), pp. 1878–1896. DOI: 10.1175/2011JCLI3621.1.

Dole, R, M Hoerling, J Perlwitz, J Eischeid, P Pegion, T Zhang, X W Quan, T Xu, and D Murray (2011). "Was there a basis for anticipating the 2010 Russian heat wave?" In: *Geophysical Research Letters* 38, p. L06702. DOI: 10.1029/2010GL046582.

Dommenget, D and M Latif (2002). "A cautionary note on the interpretation of EOFs". In: *Journal of Climate* 15 (2), pp. 216–225. DOI: 10.1175/1520-0442(2003)016<1087:COACNO>2.0.CO;2.

Douville, H, S Bielli, C Cassou, M Déqué, N M J Hall, S Tyteca, and A Voldoire (2011). "Tropical influence on boreal summer mid-latitude stationary waves". In: *Climate Dynamics* 37, pp. 1783–1798. DOI: 10.1007/s00382-011-0997-1.

Duchez, A, E Frajka-Williams, S A Josey, D G Evans, J P Grist, R Marsh, G D McCarthy, B Sinha, D I Berry, and J J-M Hirschi (2016). "Drivers of exceptionally cold North Atlantic Ocean temperatures and their link to the 2015 European heat wave". In: *Environmental Research Letters* 11 (7), p. 074004. DOI: 10.1088/1748-9326/11/7/074004.

Enfield, D B, A M Mestas-Nuñez, and P J Trimble (2001). "The Atlantic Multidecadal Oscillation and its Relationship to Rainfall and River Flows in the Continental U.S." In: *Geophysical Research Letters* 28 (10), pp. 2077–2080. DOI: 10.1029/2000GL012745.

Fink, A H, T Brücher, A Krüger, G C Leckebusch, J G Pinto, and U Ulbrich (2004). "The 2003 European summer heatwaves and drought – synoptic diagnosis and impacts". In: *Weather - Royal Meteorological Society* 59 (8), pp. 209–216. DOI: 10.1256/wea.73.04.

Folland, C K, J Knight, H W Linderholm, D Fereday, S Ineson, and J W Hurrel (2009). "The summer North Atlantic oscillation: Past, present, and future". In: *Journal of Climate* 22, pp. 1082–1102. DOI: 10.1175/2008JCLI2459.1.

Gastineau, G and C Frankignoul (2015). "Influence of the North Atlantic SST variability on the atmospheric circulation during the twentieth century". In: *Journal of Climate* 28 (4), pp. 1396–1416. DOI: 10.1175/JCLI-D-14-00424.1.

Greatbatch, R J and P P Rong (2006). "Discrepancies between different northern hemisphere summer atmospheric data products". In: *Journal of Climate* 19, pp. 1261–1273. DOI: 10.1175/JCLI3643.1.

Greatbatch, R J, G Gollan, T Jung, and T Kunz (2012). "Factors influencing Northern Hemisphere winter mean atmospheric circulation anomalies during the period 1960/61 to 2001/02". In: *Quarterly Journal of the Royal Meteorological Society* 138, pp. 1970–1982. DOI: 10.1002/qj.1947.

— (2015). "Tropical origin of the severe european winter of 1962/1963". In: *Quarterly Journal of the Royal Meteorological Society* 141, pp. 153–165. DOI: 10.1002/qj.2346.

Hall, R J, J M Jones, E Hanna, A A Scaife, and R Erdélyi (2016). "Drivers and potential predictability of summer time North Atlantic polar front jet variability". In: *Climate Dynamics*, pp. 1–19. DOI: 10.1007/s00382-016-3307-0.

Hansen, F, R J Greatbatch, G Gollan, T Jung, and A Weisheimer (2017). "Remote control on NAO predictability via the stratosphere". In: *Quarterly Journal of the Royal Meteorological Society* 143, pp. 706–719. DOI: 10.1002/qj.2958.

Hoskins, B J and T Ambrizzi (1993). "Rossby Wave Propagation on a Realistic Longitudinally Varying Flow". In: *Journal of the Atmospheric Sciences* 50 (12), pp. 1661–1671.

Hurrell, J W and C Deser (2010). "North Atlantic climate variability: The role of the North Atlantic Oscillation". In: *Journal of Marine Systems* 79 (3-4), pp. 231–244. DOI: 10.1016/j.jmarsys.2009.11.002.

Hurrell, J W, Y Kushnir, G Ottersen, and M Visbeck (2003). "An overview of the North Atlantic Oscillation". In: *The North Atlantic Oscillation: Climatic Significance and Environmental Impact, Geophysical Monograph Series*. Vol. 134. American Geophysical Union, pp. 1–35. DOI: 10.1029/GM134.

Ineson, S and A A Scaife (2009). "The role of the stratosphere in the European climate response to El Niño". In: *Nature Geoscience* 2, pp. 32–36. DOI: 10.1038/NGEO381.

Jung, T, M J Miller, and T N Palmer (2010a). "Diagnosing the Origin of Extended-Range Forecast Errors". In: *Monthly Weather Review* 138, pp. 2434–2446. DOI: 10.1175/2010MWR3255.1.

Jung, T, T N Palmer, M J Rodwell, and S Serrar (2010b). "Understanding the Anomalously Cold European Winter of 2005/06 Using Relaxation Experiments". In: *Monthly Weather Review* 138, pp. 3157–3174. DOI: 10.1175/2010MWR3258.1.

Knight, J R, C K Folland, and A A Scaife (2006). "Climate impacts of the Atlantic multidecadal oscillation". In: *Geophysical Research Letters* 33 (17), pp. 2–5. DOI: 10.1029/2006GL026242.

Lau, W K M and K-M Kim (2012). "The 2010 Pakistan Flood and Russian Heat Wave: Teleconnection of Hydrometeorological Extremes". In: *Journal of Hydrometeorology* 13 (1), pp. 392–403. DOI: 10.1175/JHM-D-11-016.1.

Li, X, E P Gerber, D M Holland, and C Yoo (2015). "A Rossby wave bridge from the tropical Atlantic to West Antarctica". In: *Journal of Climate* 28 (6), pp. 2256–2273. DOI: 10.1175/JCLI-D-14-00450.1.

Lin, H (2009). "Global Extratropical Response to Diabatic Heating Variability of the Asian Summer Monsoon". In: *Journal of the Atmospheric Sciences* 66, pp. 2697–2713. DOI: 10.1175/2009JAS3008.1.

Lin, H and Z Wu (2012). "Indian summer monsoon influence on the climate in the North Atlantic-European region". In: *Climate Dynamics* 39, pp. 303–311. DOI: 10.1007/s00382-011-1286-8.

Lorenz, E N (1956). "Empirical Orthogonal Functions and Statistical Weather Prediction". In: *Technical Report, Statistical Forecasting Project Report 1, Dept. of Meteorology, MIT*, 49pp.

North, G R, T L Bell, and R F Cahalan (1982). "Sampling Errors in the Estimation of Empirical Orthongonal Functions". In: *Monthly Weather Review* 110, pp. 699–706.

Palmer, T N and D L T Anderson (1994). "The prospects for seasonal forecasting - A review paper". In: *Quarterly Journal of the Royal Meteorological Society* 120 (518), pp. 755–793.

Parker, D E, T P Legg, and C K Folland (1992). "A new daily central England temperature series, 1772-1991". In: *International Journal of Climatology* 12 (4), pp. 317–342. DOI: 10.1002/joc.3370120402.

Reichler, T, M Dameris, and R Sausen (2003). "Determining the tropopause height from gridded data". In: *Geophysical Research Letters* 30 (20). DOI: 10.1029/2003GL018240.

Sardeshmukh, P D and B J Hoskins (1988). "The Generation of Global Rotational Flow by Steady Idealized Tropical Divergence". In: *Journal of the Atmospheric Sciences* 45 (7), pp. 1228–1251. DOI: 10.1175/1520-0469(1988)045<1228:TGOGRF>2.0.CO;2.

Schär, C and G Jendritzky (2004). "Hot news from summer 2003". In: *Nature* 432, pp. 559–560. DOI: 10.1038/432559a.

Schlesinger, M E and N Ramankutty (1994). "An oscillation in the global climate system of period 65–70 years". In: *Nature* 367 (6465), pp. 723–726. DOI: 10.1038/367723a0.

Screen, J (2013). "Influence of Arctic sea ice on European summer precipitation". In: *Environmental Research Letters* 8 (4), p. 044015. DOI: 10.1088/1748-9326/8/4/044015.

Shaw, T A, J Perlwitz, and N Harnik (2010). "Downward wave coupling between the stratosphere and troposphere: The importance of meridional wave guiding and comparison with zonal-mean coupling". In: *Journal of Climate* 23 (23), pp. 6365–6381. DOI: 10.1175/2010JCLI3804.1.

Shimizu, M H and I F de Albuquerque Cavalcanti (2011). "Variability patterns of Rossby wave source". In: *Climate Dynamics* 37 (3), pp. 441–454. DOI: 10.1007/s00382-010-0841-z.

Shukla, J, J Anderson, D Baumhefner, C Brankovic, Y Chang, E Kalnay, L Marx, T Palmer, D Paolino, J Ploshay, S Schubert, D Straus, M Suarez, and J Tribbia (2000). "Dynamical Seasonal Prediction". In: *Bulletin of the American Meteorological Society* 81 (11), pp. 2593–2606. DOI: 10.1175/1520-0477(2000)081<2593:DSP>2.3.CO;2.

Sun, X, R J Greatbatch, W Park, and M Latif (2010). "Two major modes of variability of the East Asian summer monsoon". In: *Quarterly Journal of the Royal Meteorological Society* 136, pp. 829–841. DOI: 10.1002/qj.635.

Sutton, R T and D L R Hodson (2005). "Atlantic Ocean Forcing of North American and European Summer Climate". In: *Science* 309 (115), pp. 115–118. DOI: 10.1126/science.1109496.

Trenberth, K E, G W Branstator, D Karoly, a Kumar, N C Lau, and C Ropelewski (1998). "Progress during TOGA in understanding and modeling global teleconnections associated with tropical sea surface temperatures". In: *Journal of Geophysical Research-Oceans* 103 (C7), pp. 14291–14324. DOI: 10.1029/97jc01444.

von Storch, H and A Navarra (1995). *Analysis of Climate Variability*. Springer Verlag.

von Storch, H and F W Zwiers (1999). *Statistical Analysis in Climate Research:* Cambridge: Cambridge University Press, Cambridge. DOI: 10.1017/CBO9780511612336.

Wang, B and Z Fan (1999). "Choice of South Asian Summer Monsoon Indices". In: *Bulletin of the American Meteorological Society* 80 (4), pp. 629–638. DOI: 10.1175/1520-0477(1999)080<0629:COSASM>2.0.CO;2.

Wang, B, R Wu, and K-M Lau (2001). "Interannual Variability of the Asian Summer Monsoon : Contrasts between the Indian and the Western North Pacific – East Asian Monsoons". In: *Journal of Climate* 14, pp. 4073–4090. DOI: 10.1175/1520-0442(2001)014<4073:IVOTAS>2.0.CO;2.

Weisheimer, A, F J Doblas-Reyes, T Jung, and T N Palmer (2011). "On the predictability of the extreme summer 2003 over Europe". In: *Geophysical Research Letters* 38, p. L05704. DOI: 10.1029/2010GL046455.

Xie, P and P A Arkin (1997). "Global Precipitation: A 17-Year Monthly Analysis Based on Gauge Observations, Satellite Estimates, and Numerical Model Outputs". In: *Bulletin of the American Meteorological Society* 78 (11), pp. 2539–2558. DOI: 10.1175/1520-0477(1997)078<2539:GPAYMA>2.0.CO;2.

Yin, X, A Gruber, and P Arkin (2004). "Comparison of the GPCP and CMAP Merged Gauge–Satellite Monthly Precipitation Products for the Period 1979–2001". In: *Journal of Hydrometeorology* 5 (6), pp. 1207–1222. DOI: 10.1175/JHM-392.1.

Acknowledgements

The relaxation experiments were carried out by Thomas Jung, Gereon Gollan, Felicitas Hansen and Richard Greatbatch and the model was provided by the ECMWF.

The NOAA/OAR/ESRL PSD, Boulder, Colorado, USA provided the CMAP data on their website http://www.esrl.noaa.gov/psd/

The PJ index was provided by Xinyu Li.

The manuscript was typeset in LaTeX. The template for it has been modified and has been downloaded in its original version from http://www.LaTeXTemplates.com with the license CC BY-NC-SA 3.0 (http://creativecommons.org/licenses/by-nc-sa/3.0/).

All analyses have been carried out in python. Special credit goes to A. Dawson for providing the EOF package (Dawson, 2016a) and the windspharm package (Dawson, 2016b) which were of great help for my work.

I want to thank Richard Greatbatch and Daniela Domeisen for the supervision of this thesis. I greatly appreciate the time that they invested to discuss the work with me and the many helpful comments they provided. Thanks go also to Gereon and Felicitas who participated in many discussions and helped me get started with the data.

I further want to give credit to Katherine, Milan and Eike for always being there and willing to help and discuss any issues that I ran into. I especially want to thank Milan and Katherine for proofreading large parts of this thesis and thus helping me to improve this manuscript.

And last but not least, to my family: thanks for always supporting me in every possible way throughout the course of my studies.

Erklärung

Hiermit erkläre ich, dass ich die vorliegende Arbeit selbständig und ohne fremde Hilfe angefertigt und keine anderen als die angegebenen Quellen und Hilfsmittel verwendet habe. Die eingereichte schriftliche Fassung der Arbeit entspricht der auf dem elektronischen Speichermedium. (Name der Datei: `Wulff_5478.pdf`)
Weiterhin versichere ich, dass diese Arbeit noch nicht als Abschlussarbeit an anderer Stelle vorgelegen hat.

Datum, Unterschrift:

_____